COMMUNICATIONS IN COMPUTATIONAL PHYSICS
Vol. **2**, No. 4, pp. 684-722

Commun. Comput. Phys.
August 2007

Fully Kinetic, Electromagnetic Particle-in-Cell Simulations of Plasma Microturbulence

J. L. V. Lewandowski* and L. E. Zakharov

Plasma Physics Laboratory, Princeton University, P.O. Box 451, Princeton, NJ 08543, USA.

Received 13 November 2006; Accepted (in revised version) 3 December 2006

Available online 15 January 2007

Abstract. A novel numerical method, based on physical intuition, for particle-in-cell simulations of electromagnetic plasma microturbulence with fully kinetic ion and electron dynamics is presented. The method is based on the observation that, for low-frequency modes of interest [$\omega/\omega_{ci} \ll 1$, ω is the typical mode frequency and ω_{ci} is the ion cyclotron frequency] the impact of particles that have velocities larger than the resonant velocity, $v_r \sim \omega/k_\parallel$ ($k_\parallel$ is the typical parallel wavenumber) is negligibly small (this is especially true for the electrons). Therefore it is natural to analytically segregate the electron response into an adiabatic response and a nonadiabatic response and to numerically resolve only the latter: this approach is termed the splitting scheme. However, the exact separation between adiabatic and nonadiabatic responses implies that a set of coupled, nonlinear elliptic equations has to be solved; in this paper an iterative technique based on the multigrid method is used to resolve the apparent numerical difficulty. It is shown that the splitting scheme allows for clean, noise-free simulations of electromagnetic drift waves and ion temperature gradient (ITG) modes. It is also shown that the advantage of noise-free kinetic simulations translates into better energy conservation properties.

PACS (2006): 52.35Kt, 52.30Jb, 52.35Ra

Key words: Plasma micro-turbulence, particle-in-cell simulation, multigrid solver.

1 Introduction

There is growing experimental [2, 3] and theoretical [4, 6] evidence that the so-called anomalous (cross-field) transport observed in toroidal fusion devices is due to microturbulence (for a good review on the topic of anomalous transport, the reader should consult

*Corresponding author. *Email addresses:* jlewando@pppl.gov (J. L. V. Lewandowski), zakharov@pppl.gov (L. E. Zakharov)

the paper by Horton [5] and references therein). Although there is now a good understanding of the basic mechanisms of small-scale, low-frequency turbulence in tokamak and stellarator plasmas [7], the actual numerical modeling of such turbulent plasmas is lagging behind the theory. In particular most numerical studies rely on the assumption that the electrons respond adiabatically to the waves; such an assumption is of course very useful but also implies not addressing some key physical effects associated with kinetic (non-adiabatic) electrons.

In order to take into account wave-particle interactions and nonlinear wave effects [8] we adopt the particle-in-cell (PIC) simulations approach to simulate the ion dynamics *and* the electron dynamics. As it is well known, in view of the large mass ratio, $m_i/m_e \gg 1$, the PIC simulation of electron dynamics suggests the use of a very small time step of integration. However our main interest is to simulate low-frequency ($\omega/\omega_{ci} \ll 1$), drift-type ($k_{||}/k_{\perp} \ll 1$) modes for which the bulk of the electrons respond adiabatically to the waves [4,5]. Therefore it may prove advantageous to focus on the *nonadiabatic* part of the electron response rather than on the entire electron response: this is the basic idea of the splitting scheme. In the electrostatic case the splitting scheme has been shown to be more accurate in the linear regime [26] (e.g. linear growth rates) and in the nonlinear regime [1] (e.g. energy conservation in the saturated state) than the conventional δf scheme [10,11].

This paper presents a generalization of the splitting scheme to the electromagnetic case. The electromagnetic splitting scheme is a natural extension of the electrostatic version of the scheme [26]; however there are new numerical difficulties that require special consideration. In addition, we show how to account for collisional effects (which were neglected in the electrostatic case [1,26]) in the splitting scheme.

The paper is organized as follows. In Section 2, the derivation of the electromagnetic splitting scheme is presented and, for the sake of comparison, the model equations for the conventional δf method are also given. The equations governing the required scalar fields (e.g. electrostatic potential) are also presented in the same section. Section 3 is devoted to linear benchmarks. A potential numerical instability is discussed in detail in Section 4. Nonlinear simulations of electromagnetic drift waves using the splitting scheme are presented in Section 5. Concluding remarks are given in Section 6.

2 Splitting scheme for electromagnetic turbulence

2.1 Basic method

The distribution function for particle species j, denoted F_j, is governed by the collisional, gyrokinetic Vlasov equation (in the long-wavelength limit)

$$\frac{dF_j}{dt} \equiv \frac{\partial F_j}{\partial t} + \left(v_{\|}\widehat{\mathbf{b}} + \mathbf{V}_E\right)\cdot\boldsymbol{\nabla} F_j + \frac{q_j}{m_j} E_{\|}\frac{\partial F_j}{\partial v_{\|}} = C_j(F_j)\,, \tag{2.1}$$

where

$$\begin{aligned}
&\widehat{\mathbf{b}} \equiv \widehat{\mathbf{b}}_0 + \frac{\delta \mathbf{B}_\perp}{B_0} \equiv \widehat{\mathbf{b}}_0 + \frac{\boldsymbol{\nabla} A_\parallel \times \widehat{\mathbf{b}}_0}{B_0} \ , \\
&\mathbf{V}_E = c \frac{\widehat{\mathbf{b}}_0 \times \boldsymbol{\nabla} \Phi}{B_0} \ , \\
&E_\parallel \equiv -\widehat{\mathbf{b}} \cdot \boldsymbol{\nabla} \psi \equiv -\widehat{\mathbf{b}} \cdot \boldsymbol{\nabla} \Phi - \frac{1}{c} \frac{\partial A_\parallel}{\partial t} \ ,
\end{aligned} \tag{2.2}$$

and $\widehat{\mathbf{b}}_0 \equiv \mathbf{B}_0 / B_0$ is a unit vector in the direction of the equilibrium (unperturbed) magnetic field, q_j is the charge of species j, m_j is the mass of species j, Φ is the electrostatic potential, $A_\parallel$ is the parallel component of the magnetic vector potential, and ψ is termed the generalized magnetic potential. The confining magnetic field is taken to be of the form $\mathbf{B}_0 = B_0(\widehat{\mathbf{z}} + \theta \widehat{\mathbf{y}})$ where $\theta \ll 1$ is a small parameter describing the pitch of the magnetic field (since we are restricting ourselves to a one-dimensional approximation, the gradient in the direction of the equilibrium magnetic field is simply $\nabla_{||} \widetilde{f} = \theta \partial \widetilde{f} / \partial y$). The collision operator on the right-hand side of Eq. (2.1) is quite general and its explicit form is not yet specified but we shall assume, however, that it does satisfy the basic requirements that: (a) it annihilates a Mawxwellian distribution F_{Mj} with density n_0 and temperature T_j, $C_j(F_{Mj}) = 0$; and (b) it conserves the particle number, $\int C_j(F_j) dv_\parallel = 0$. One can of course demand that the collision operator satisfies additional properties, such as the conservation of momentum and energy. As it is customary in PIC simulations, the collisional effects are treated perturbatively, and we first consider Eq. (2.1) in the collisionless limit. For clarity, we introduce the following operators

$$\begin{aligned}
&L_0 \equiv \frac{\partial}{\partial t} + v_\parallel \widehat{\mathbf{b}}_0 \cdot \boldsymbol{\nabla} \ , \\
&\widehat{L}_j \equiv \mathbf{V}_\phi \cdot \boldsymbol{\nabla} + \frac{q_j}{m_j} E_\parallel \frac{\partial}{\partial v_\parallel} \ ,
\end{aligned} \tag{2.3}$$

where $\mathbf{V}_\phi = c \mathbf{B}_0 \times \boldsymbol{\nabla} \phi / B_0^2$ and $\phi \equiv \Phi - v_\parallel A_\parallel / c$. In the collisionless limit, Eq. (2.1) then reduces to

$$\frac{dF_j}{dt} = L_0(F_j) + \widehat{L}_j(F_j) = 0.$$

The electrostatic potential, Φ, and the parallel component of the magnetic vector potential, $A_\parallel$, can be determined using the gyro-kinetic Poisson equation (in the long-wavelength limit)

$$\frac{e^2}{T_e} n_0 \rho_s^2 \nabla_\perp^2 \Phi = -\rho \, , \tag{2.4}$$

and Ampère's law

$$\nabla_\perp^2 A_\parallel = -\frac{4\pi}{c} J_\parallel \, , \tag{2.5}$$

where $\nabla_\perp^2 \equiv (\boldsymbol{\nabla} - \widehat{\mathbf{b}}_0(\widehat{\mathbf{b}}_0 \cdot \boldsymbol{\nabla}))^2$ is the perpendicular Laplacian and

$$\rho = \sum_j q_j \int_{-\infty}^{+\infty} F_j dv_\parallel \,, \quad J_\parallel = \sum_j q_j \int_{-\infty}^{+\infty} v_\parallel F_j dv_\parallel \,.$$

Here $\rho_s = c_s/\omega_{ci}$ is the ion thermal velocity evaluated at the electron temperature, $c_s = \sqrt{T_e m_i}$ and $\omega_{ci} = eB_0/(m_i c)$. Before presenting the electromagnetic version of the splitting scheme we briefly derive the model equations based on the conventional δf method [10, 11]. Following the standard procedure the distribution function is written as $F_j = F_{Mj} + \delta f_j$; noting that $L_0(F_{Mj}) = 0$ it follows that the perturbed part of the distribution function satisfies the equation of

$$\frac{d\delta f_j}{dt} = -\widehat{L}_j(F_{Mj}) \,,$$

and the corresponding dynamical equation for the weight $W_j \equiv \delta f_j / F_j$ is

$$\frac{dW_j}{dt} = (1 - W_j)\left(\boldsymbol{\kappa}_j \cdot \mathbf{V}_\phi + \frac{q_j}{T_j}\, E_\parallel v_\parallel\right), \tag{2.6}$$

where $\boldsymbol{\kappa}_j = \boldsymbol{\kappa}[1 - \eta_j(1 - \overline{v}_\parallel^2)/2]$, $\boldsymbol{\kappa} = -\boldsymbol{\nabla} n_0/n_0$, $\overline{v}_\parallel = v_\parallel / V_{\mathrm{th}j}$ and $V_{\mathrm{th}j} = \sqrt{T_j/m_j}$. The equations of motion for the k^{th} marker, which is specified through its coordinates in phase space $(\mathbf{x}_k(t), v_{\parallel k}(t))$ are

$$\left.\begin{aligned} \frac{d\mathbf{x}_k}{dt} &= v_{\parallel k}\widehat{\mathbf{b}}_0 + \left(\mathbf{V}_\phi\right)_{\mathbf{x}_k, v_{\parallel k}} , \\ \frac{dv_{\parallel k}}{dt} &= \frac{q_j}{m_j}\, \left(E_\parallel\right)_{\mathbf{x}_k} . \end{aligned}\right\} \tag{2.7}$$

We now proceed to derive the splitting scheme for electromagnetic simulations. Following the same methodology as in the electrostatic case [26] we write the following Ansatz for the distribution function for species j

$$F_j = H_j(\psi) F_{Mj} + h_j \,, \tag{2.8}$$

where h_j denotes the nonadiabatic response and $H_j(\psi)$ is a yet unknown function of the generalized magnetic potential. Upon substitution of Eq. (2.8) in Eq. (2.1) one obtains the following dynamical equation for the nonadiabatic response

$$\frac{dh_j}{dt} + \left[H_j'\left(\frac{\partial}{\partial t} + \mathbf{V}_E \cdot \boldsymbol{\nabla}\right)\psi - H_j \boldsymbol{\kappa}_j \cdot \mathbf{V}_\phi\right] F_{Mj} - v_\parallel E_\parallel \left\{H_j' + \frac{q_j}{T_j}\, H_j\right\} F_{M_j} = 0 \,, \tag{2.9}$$

where $\boldsymbol{\kappa}_j \equiv -\boldsymbol{\nabla} F_{Mj}/F_{Mj}$ and a prime denotes a derivative with respect to ψ. As in the electrostatic version of the splitting scheme [26], we demand that the term which multiplies the parallel acceleration force vanishes; this is equivalent to demanding that the

term between curly brackets in Eq. (2.9) vanishes implying the equation

$$\frac{dH_j}{d\psi} + \frac{q_j}{T_j} H_j = 0,$$

which admits the solution of $H_j(\psi) = e^{-q_j\psi/T_j}$. It follows immediately that the distribution function for species j is

$$F_j = e^{-q_j\psi/T_j} F_{Mj} + h_j. \tag{2.10}$$

The above equation is the essence of the electromagnetic splitting scheme. In the same spirit as in the electrostatic version of the scheme [26], the relevant dynamics are now contained in the weight dynamical equation associated with the *nonadiabatic* part of the distribution function; specifically, introducing $W_j^{(\mathrm{NA})} \equiv h_j / F_j$, and using Eq. (2.1) with the representation (2.10), one arrives at

$$\frac{dW_j^{(\mathrm{NA})}}{dt} = \left(1 - W_j^{(\mathrm{NA})}\right) \left[\boldsymbol{\kappa}_j \cdot \mathbf{V}_\phi + \frac{q_j}{T_j} \left(\varphi + \mathbf{V}_E \cdot \boldsymbol{\nabla}\psi\right)\right], \tag{2.11}$$

where $\varphi \equiv \partial\psi/\partial t$. Two remarks are in order: first, by construction, the contribution due to the parallel free streaming are absent in the weight equation (2.11); second, in analogy with the electrostatic case, the quantity φ is treated as a distinct scalar field. Apart from the electrostatic potential, Φ, and the parallel component of the magnetic vector, $A_\parallel$, which are obtained by solving Eqs. (2.4) and (2.5) respectively, the splitting scheme also requires the computation of the following scalar fields: $E_{||}$ for the equation of motion and $\varphi = \partial\psi/\partial t$ for the weight equation.

2.2 Field equations for the splitting scheme

The general procedure to derive the various field equations is similar to that outlined in a previous paper [26]. The general idea is to treat φ in the weight equation, Eq. (2.11), as a separate scalar field rather than using a finite-difference method for $\partial\psi/\partial t$ (which could be numerically unstable). In turn the scalar fields are determined by taking velocity moments of Eq. (2.1), the gyrokinetic Poisson equation and Ampère's law. The self-consistent system of equations for the various scalar fields is derived in Appendix B; all the equations given below are written in normalized gyro-kinetic units ($\omega_{\mathrm{ci}} t \mapsto t$; $(x,y)/\rho_s \mapsto (x,y)$; $v_\parallel / c_s \mapsto v_\parallel$; $e\Phi/T_e \mapsto \Phi$; $e\psi/T_e \mapsto \psi$; $A_\parallel/(\rho_s B_0) \mapsto A_\parallel$; $e\varphi/(\omega_{\mathrm{ci}} T_e) \mapsto \varphi$). The gyrokinetic Poisson equation is

$$\frac{\partial^2 \Phi}{\partial y^2} = (1 + 1/\tau)\psi + \int_{-\infty}^{+\infty} (h_e - h_i) dv_\parallel - \widehat{\rho}, \tag{2.12}$$

where $\widehat{\rho} \equiv (1+1/\tau)\psi + e^{-\psi/\tau} - e^{\psi} = \mathcal{O}(|\psi|^2)$. Ampère's law takes the form of

$$\frac{\partial^2 A_\parallel}{\partial y^2} = \beta \int_{-\infty}^{+\infty} (h_e - h_i) v_\parallel dv_\parallel, \tag{2.13}$$

where $\beta \equiv 4\pi n_0 T_e / B_0^2$. The equation governing the parallel electric field is

$$\left(\frac{\partial^2}{\partial y^2} - \eta\right) E_\parallel = \nabla_{||} \int_{-\infty}^{+\infty} (h_i - h_e) dv_\parallel - \beta \nabla_{||} \int_{-\infty}^{+\infty} (h_i - h_e) {v_\parallel}^2 dv_\parallel + \beta \left[\xi \kappa_n \frac{\partial A_\parallel}{\partial y} + \sum_j Z_j C_j^{(1)} \right], \tag{2.14}$$

where $\xi \equiv \tau(1+\eta_i) - \epsilon^{-1}(1+\eta_e)$ and $\epsilon \equiv m_e/m_i \ll 1$ is the electron-to-ion mass ratio, $C_j^{(1)}$ is the first-order velocity moment of the collision operator (the exact definition is given in Appendix A) and

$$\eta \equiv \beta \left(\int_{-\infty}^{+\infty} h_i dv_\parallel + \epsilon^{-1} \int_{-\infty}^{+\infty} h_e dv_\parallel \right) + e^\psi + \frac{1}{\tau} e^{-\psi/\tau}.$$

In order to obtain an expression for $\varphi = \partial\psi/\partial t$ it is numerically convenient to seek an elliptic equation governing $\varpi \equiv \partial E_\parallel / \partial t$; a simple integration along the equilibrium magnetic field line

$$\varphi(y,t) = -\theta^{-1} \int^y \varpi(y',t) dy', \tag{2.15}$$

provides the required quantity. The elliptic equation governing ϖ is

$$\left[\frac{\partial^2}{\partial y^2} - \beta(\sigma + \sigma_0)\right] \varpi = \nabla_{||}^2 \left[\beta \int_{-\infty}^{+\infty} (h_i - h_e) {v_\parallel}^3 dv_\parallel - \int_{-\infty}^{+\infty} (h_i - h_e) v_\parallel dv_\parallel \right] - \beta \xi \kappa_n \frac{\partial E_\parallel}{\partial y} + S_c + S_{\rm NL}, \tag{2.16}$$

where

$$\sigma_0 = 1 + 1/\epsilon, \quad \sigma = \epsilon^{-1} \left[e^\psi - 1 + \int_{-\infty}^{+\infty} h_e dv_\parallel \right] + e^{-\psi/\tau} - 1 + \int_{-\infty}^{+\infty} h_i dv_\parallel, \tag{2.17}$$

and

$$\begin{aligned} S_c &= \beta \left[\frac{\partial}{\partial t} \left(\sum_j Z_j C_j^{(1)} \right) - \nabla_\parallel \left(\sum_j Z_j C_j^{(2)} \right) \right], \\ S_{\rm NL} &= \beta \left[\left(\sigma_0 \mathbf{V}_E \cdot \boldsymbol{\kappa} - \nabla_{||} \widehat{\sigma} \right) E_\parallel - 2 \nabla_{||} \left(\widehat{\sigma} E_\parallel \right) \right], \\ \widehat{\sigma} &= \int_{-\infty}^{+\infty} h_i v_\parallel dv_\parallel + \epsilon^{-1} \int_{-\infty}^{+\infty} h_e v_\parallel dv_\parallel. \end{aligned} \tag{2.18}$$

The term $S_{\rm NL}$ accounts for quadratic nonlinearities in the scalar fields and the impact of collisional effects are given by the term labeled $S_{\rm c}$. We note that the solution of Eq. (2.12) for the electrostatic potential is dependent on the generalized magnetic potential, ψ. In

turn the generalized magnetic potential requires the solution of Eq. (2.14) for the parallel electric field since

$$\psi(y,t) = -\theta^{-1} \int^{y} E_{\parallel}(y',t)dy' . \tag{2.19}$$

Note that the term η on the left-hand side of Eq. (2.14) also depends on ψ; based on these observations, one can outline a numerical procedure for the self-consistent solution of the above system of equations. In the first step, one solves Ampère's law, Eq. (2.13), for $A_{||}$. In the second step, assuming an initial guess for ψ (say $\psi^{(0)}$), one solves Eq. (2.14) for the parallel electric field and a new approximation, $\psi^{(1)}$, can be obtained using Eq. (2.19); the approximation $\psi^{(1)}$ is then used in Eq. (2.14) and a new approximation $\psi^{(2)}$ is found: this process can be repeated a few times until an appropriate convergence criterion between two consecutive iterations has been reached (for example, $||\psi^{(\ell+1)}-\psi^{(\ell)}||/||\psi^{(\ell)}|| < \delta$ where $\delta \ll 1$ is a small prescribed parameter, $||\bullet||$ is a suitable norm and ℓ denotes the iteration number); the knowledge of the generalized magnetic potential ψ allows us to solve the gyrokinetic Poisson equation, Eq. (2.12), for the electrostatic potential, followed by the solution of Eq. (2.16) for ϖ and Eq. (2.15) for $\varphi = \partial\psi/\partial t$. However, it is has been found numerically that the procedure just outlined converges rather slowly, and sometimes fails to converge altogether. Therefore we have devised an alternative numerical procedure. Subtracting $(1+1/\tau)\Phi$ from both sides of Eq. (2.12)

$$\left[\frac{\partial^2}{\partial y^2} - (1+1/\tau)\right]\Phi = (1+1/\tau)\mathsf{U} + \int_{-\infty}^{+\infty}(h_e - h_i)dv_{\parallel} - \widehat{\rho}, \tag{2.20}$$

where

$$\mathsf{U} \equiv \psi - \Phi = \theta^{-1}\int^{y}\chi(y',t)dy' , \tag{2.21}$$

and $\chi \equiv \partial A_{\parallel}/\partial t$ is a new scalar field. The elliptic equation governing χ is derived in Appendix A:

$$\begin{aligned}\frac{\partial^2\chi}{\partial y^2} = \beta\nabla_{||}\left[\int_{-\infty}^{+\infty}(h_i - h_e){v_{\parallel}}^2 dv_{\parallel} - \kappa_n\xi\frac{\partial A_{\parallel}}{\partial y} - \sum_j Z_j C_j^{(1)}\right] \\ -\beta\left[\int_{-\infty}^{+\infty}h_i dv_{\parallel} + \epsilon^{-1}\int_{-\infty}^{+\infty}h_e dv_{\parallel}\right]E_{\parallel} .\end{aligned} \tag{2.22}$$

Note that the last term on the right-hand side of the above equation involves quadratic nonlinearities of perturbed quantities. The set of equations (2.7), (2.11), (2.13)-(2.22) forms a self-consistent system suitable for simulating electromagnetic microturbulence in the presence of kinetic electrons. In order to describe the explicit form of the algorithm used in solving the field equations in the electromagnetic splitting scheme, we adopt a simplified notation for each elliptic equation; for example, $\chi = \chi(A_{\parallel}, E_{\parallel}, y)$ stands for Eq. (2.22).

Using this notation, the numerical algorithm is then:

Step 1. Solve Ampère's law: $A_{||}=A_{||}(y)$.

Step 2. Set $\psi=\psi^{(0)}$ [initial guess; say $\psi^{(0)}=\Phi$ or $\psi^{(0)}=\psi(t-\Delta t)$] .

Step 3. Solve for ψ and $E_{||}$ iteratively:

$$\left.\begin{aligned} E_{||}^{(\ell+1)} &= E_{||}(A_{||},\psi^{(\ell)},y) \\ \psi^{(\ell+1)} &= -\theta^{-1}\int^{y} E_{||}^{(\ell+1)}(y',t)dy' \end{aligned}\right\} \ell=0,1,\cdots,M-1$$

Step 4. Set $E_{||}=E_{||}^{(M)}$ and $\psi\equiv\psi^{(M)}$, and solve:

$$\begin{aligned} &\chi\equiv\frac{\partial A_{||}}{\partial t}=\chi(A_{||},E_{||},y), \quad \mathsf{U}\equiv\psi-\Phi=\theta^{-1}\int^{y}\chi(y',t)dy', \\ &\Phi=\Phi(\mathsf{U},\psi,y), \quad \varpi\equiv\frac{\partial E_{||}}{\partial t}=\varpi(E_{||},\psi,y), \\ &\varphi\equiv\frac{\partial\psi}{\partial t}=-\theta^{-1}\int^{y}\varpi(y',t)dy'. \end{aligned}$$

The number of iterations required for the set $\{\psi,E_{\|}\}$ (step **3** above) is small; typically $M=2$ or $M=3$ is sufficient. Our approach is based on the exact separation between the adiabatic response and the nonadiabatic response (see Eq. (2.10)) for both the electron population and the ion population. However in some applications it is possible to use the δf scheme for the ion dynamics while the representation (2.10) remains appropriate for the electron dynamics.

2.3 Field equations for the δf scheme

In the next section, we shall make some comparisons with the numerical properties of the conventional δf scheme. The conventional electromagnetic δf scheme requires the solution of three elliptic equations for (Φ, $A_{\|}$, $E_{\|}$); the methodology for the derivation of these elliptic equations is similar to that described in Appendix A and we omit the algebraic details. The required elliptic equations governing Φ, $A_{\|}$ and $E_{\|}$ are:

$$\frac{\partial^2\Phi}{\partial y^2}=-\int_{-\infty}^{+\infty}(\delta f_i-\delta f_e)dv_{\|}\,, \tag{2.23}$$

$$\frac{\partial^2 A_{\|}}{\partial y^2}=-\beta\int_{-\infty}^{+\infty}(\delta f_i-\delta f_e)v_{\|}dv_{\|}\,, \tag{2.24}$$

and

$$\left[\frac{\partial^2}{\partial y^2}-\beta(\sigma+\sigma_0)\right]E_\parallel$$
$$=\nabla_\parallel\int_{-\infty}^{+\infty}(\delta f_i-\delta f_e)dv_\parallel+\beta\left[\xi\kappa_n\frac{\partial A_\parallel}{\partial y}-\nabla_\parallel\int_{-\infty}^{+\infty}(\delta f_i-\delta f_e)v_\parallel^2 dv_\parallel+\sum_j Z_j C_j^{(1)}\right]. \quad (2.25)$$

The noticeable difference between the system of field equations for the δf scheme as compared to those for the splitting scheme is that no iterative procedure is needed. However, as for the case of the splitting scheme, the equations must be solved in a specific order; in particular Ampère's law, Eq. (2.24), must be solved *before* Eq. (2.25).

2.4 Remarks on the numerical method

The field equations for the splitting scheme and the conventional δf scheme are elliptic equations that can all be cast in the form of

$$\left(\frac{\partial^2}{\partial y^2}-A(y)\right)F(y,t)=S(y,t), \quad (2.26)$$

where $F(y,t)$ is an arbitrary scalar field (such as $A_{||}$, Φ, $E_\parallel$, etc.), $A(y)$ is a positive-definite function and $S(y,t)$ is a known source term. Note that in some cases the function A sometimes depends on other scalar fields themselves: this is the case, for example, for the elliptic equation governing the parallel electric field, Eq. (2.14). Since the configuration is assumed to be periodic in the y direction (with period L) one can solve Eq. (2.26) in Fourier space and then transform back to real space. However the presence of numerous quadratic nonlinearities in the PDEs governing the scalar fields Φ, $A_\parallel$, $E_\parallel$, ϖ and χ would require multiple convolutions in Fourier space; in some cases [see in particular the equation governing $E_{||}$ and the definition of η below Eq. (2.14)] one would need to carry out an *infinite* number of such convolutions. These observations suggest the use of the multigrid method [15–21] for solving Eq. (2.26); the one-dimensional multigrid solver was described and tested in [26]. It is important to note that the magnitude of A in the finite-difference approximation of the elliptic equation (2.26) imposes a constraint on the grid spacing. To show this consider the case $A=A_0=\text{const}>0$ and define $\lambda\equiv 1/\sqrt{A_0}$. If the grid spacing is denoted Δy, we must resolve the scale associated with λ; numerically this implies that the condition $\Delta y<\lambda$ must be satisfied. The multigrid method used in this paper is based on a set of consecutive V cycles; the basic solver on each subgrid to damp the modes (modes of the algebraic error, not physical modes!) is the weighted Jacobi solver, as in [26].

3 Linear electromagnetic simulations

The linear dispersion for modes of the form $\exp(-i\omega t+i\mathbf{k}\cdot\mathbf{x})$, based on the electromagnetic splitting scheme, is derived in Appendix B and is shown to be

$$\mathcal{D}(\omega,k)=\omega b+(1-\beta\Omega^2)\left[\omega(1+1/\tau)+\sum_j Z_j\zeta_j\mathcal{R}(\zeta_j)\right]=0, \tag{3.1}$$

where $b\equiv k_\perp^2\rho_s^2$, $\Omega\equiv\omega/(k_\parallel c_s)$, $\beta\equiv 4\pi e n_0 T_e/B_0^2$,

$$\mathcal{R}(\zeta_j)\equiv\frac{\omega_\star}{\zeta_j}\,(1+\eta_j\zeta_j^2)+Z(\zeta_j)\left[\omega\theta_j+\omega_\star\left(1-\eta_j/2+\eta_j\zeta_j^2\right)\right],$$

$\zeta_j=\omega/(\sqrt{2}k_\parallel V_{thj})$, $\theta_j\equiv Z_jT_e/T_j$, $\omega_\star=(k_y\rho_s)c_s/L_n$ is the drift frequency, $\eta_j\equiv L_n/L_{T_j}$ and $Z(\zeta)$ is the plasma dispersion function with complex argument ζ of Fried and Conte [14]. Before considering the linear benchmark with the complete dispersion relation, Eq. (3.1), we first study the normal modes of the system for $\omega_\star\equiv 0$; in this limit the dispersion relation (3.1) simplifies to

$$b+(1-\beta\Omega^2)\left[1+\tau^{-1}+\tau^{-1}\zeta_iZ(\zeta_i)+\zeta_eZ(\zeta_e)\right]=0. \tag{3.2}$$

For the case of a simulated plasma with cold ions and warm electrons, $\zeta_e\ll 1\ll\zeta_i$, one can expand the plasma dispersion function [14] in the appropriate limits; assuming that $\beta\Omega^2\gg 1$ one obtains the real mode frequency associated with the kinetic shear-Alfvén wave

$$\omega_r=\pm k_\parallel c_s\frac{\sqrt{1+b}}{\sqrt{\beta}}\ . \tag{3.3}$$

The imaginary part of Eq. (3.2) in the appropriate limit yields the damping rate, γ, of the kinetic shear-Alfvén wave

$$\frac{\gamma}{k_\parallel c_s}=-\sqrt{\frac{\pi}{8}}\sqrt{\frac{m_e}{m_i}}\frac{b}{\beta}\ . \tag{3.4}$$

We note that both the real mode frequency and the damping rate of the kinetic shear-Alfvén wave decreases with increasing β. The numerical solution of the dispersion relation (3.1) (or, for the case $\omega_\star\equiv 0$, Eq. (3.2)) is carried out using Muller's method, which is basically a generalization of the secant method based on quadratic interpolation [22–24]. Muller's method is not self-starting and one must initially specify three points in the complex plane. Although these starting points can be selected arbitrarily it is computationally more economical to carry out the root finding procedure in the vicinity of an analytical estimate of the location of the root $(\omega_r^{(a)},\gamma^{(a)})$. Specifically we can specify two points in the complex plane which label the lower right corner (ω_{r1},γ_1) and upper left corner (ω_{r2},γ_2)

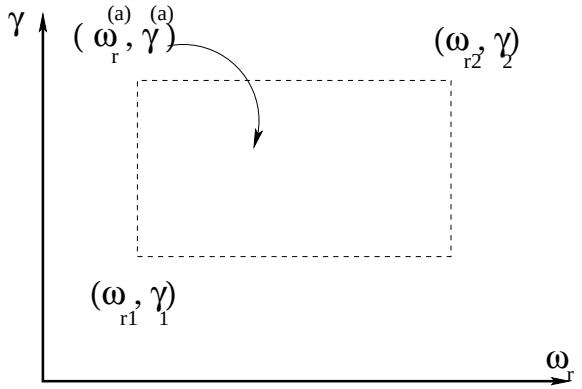

Figure 1: Given an analytical estimate for the real mode frequency, $\omega_r^{(a)}$, and for the linear growth rate, $\gamma^{(a)}$, the dispersion relation is solved using the Box-Muller algorithm in part of the complex plane defined by $\omega_{r1}<\omega_r<\omega_{r2}$ and $\gamma_1<\gamma<\gamma_2$ (represented by a closed dotted line).

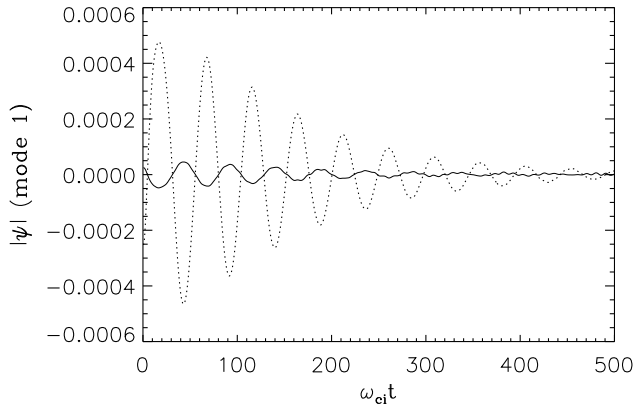

Figure 2: Time evolution of the real (plain) and imaginary (dotted) parts of the generalized magnetic potential ψ for a linear simulation of normal mode (kinetic shear Alfvèn mode) with $N_e=N_i=28657$ markers for $\beta=0.1\%$. The length of the system is $L=16\rho_s$ on a grid with $N_g=64$ grid points. The pitch of the magnetic field is $\theta=0.01$. The time step of integration is $\omega_{ci}\Delta t=0.5$.

of a rectangle that encloses $(\omega_r^{(a)},\gamma^{(a)})$; this is illustrated in Fig. 1. Muller's method is used in the triangle formed by (ω_{r1},γ_1), (ω_{r2},γ_1) and (ω_{r2},γ_2); if no root is found, then one uses Muller's method once again in the triangle formed by (ω_{r1},γ_1), (ω_{r2},γ_2) and (ω_{r1},γ_2). If an approximate location of the root(s) cannot be found then one must vary the point locations (ω_{r1},γ_1) and (ω_{r2},γ_2) such as to encompass an appropriate area of the complex plane.

Fig. 2 shows the time evolution of the real (plain) and imaginary (dotted) parts of the generalized magnetic potential ψ for a linear simulation of the kinetic shear Alfvèn wave with $N_e=N_i=28657$ markers for $\beta=0.1\%$. The length of the system is $L=16\rho_s$ on a grid with $N_g=64$ grid points. The pitch of the magnetic field is $\theta=0.01$ and the time

step of integration is $\omega_{ci}\Delta t = 0.5$; only the $n = 1$ mode, corresponding to $k_\perp \rho_s = 0.39$, is retained in the system. Fig. 3 shows the time evolution of the magnitude of the parallel component of the magnetic vector for the same simulation as in Fig. 2. The damping rate of the kinetic shear-Alfvén wave, estimated from the slope of the dashed line, is found to be $\gamma/\omega_{ci} = -0.00804$ which is in good agreement with the damping rate computed from the numerical solution of the dispersion relation (3.2), $\gamma^{(\mathrm{N})}/\omega_{ci} = -0.00809$ (here the superscript '(N)' means the given quantity has been computed numerically from the exact dispersion relation).

Fig. 4 shows the power spectrum of $|\psi^2|$ based on $N_t = 5000$ time steps. The peaks of the power spectrum in Fig. 4 are located at $\omega_r/\omega_{ci} = \pm 0.129$ in excellent agreement with the numerical solution, $\omega_r^{(\mathrm{N})}/\omega_{ci} = \pm 0.130$. A simulation with the same physical parameters and the same initial conditions using the standard δf scheme yields a damping rate which is about 10% too large, $\gamma/\omega_{ci} = -0.00892$. The inaccuracy of the δf scheme as compared to the electromagnetic splitting scheme will be discussed below. An important aspect of the electromagnetic splitting scheme is the time step of integration. A simple (numerical) stability analysis shows that the time step is constrained by the so-called Courant-Friedrichs-Lewy (CFL) criterion [9] $k_\parallel V_{\max}\Delta t < 1$ where $V_{\max}$ is a typical maximum velocity, usually of the order of the electron thermal velocity. It is important to realize that, as the number of markers in the simulated plasma is increased, the tail of the numerically-loaded distribution function becomes progressively more populated; in other words, the maximum velocity, $V_{\max}$, increases with the number of markers in the simulation. Although the markers in the tail of the distribution have a negligible impact on the low-frequency modes of interest, they do constrain the time step of integration. Our numerical experiments have shown that it is possible to use a time step marginally larger that the CFL time step, $(\Delta t)_{\mathrm{CFL}} = 1/(k_\parallel V_{\max})$, although to the detriment of numerical accuracy.

Fig. 5 shows the damping rate of the kinetic shear-Alfvén wave as a function of β for various time steps of integration. The thin plain lines with diamonds, triangles and squares show the measured damping rates for $\omega_{ci}\Delta t = 1.0$, $\omega_{ci}\Delta t = 0.5$ and $\omega_{ci}\Delta t = 0.1$, respectively. The thick dashed line represents the numerical solution of the dispersion relation, Eq. (3.2). The number of markers is $N_e = N_i = 46368$ and the total simulation time is $\omega_{ci}T = 500$; the maximum velocity at $t = 0$ is approximately 4 times the electron thermal velocity from which we conclude $\omega_{ci}(\Delta t)_{\mathrm{CFL}} \simeq 0.67$. Note that as the β value is increased both the real mode frequency, Eq. (3.3), and the damping rate, Eq. (3.4), become smaller in magnitude. Therefore if one demands good numerical accuracy for the damping rate for a large magnetic pressure (say $\beta \gtrsim 1.0\%$) one needs to use a time step of integration such that $\Delta t < (\Delta t)_{\mathrm{CFL}}$.

Fig. 6 shows a different perspective of the impact of the time step of integration on the accuracy of the electromagnetic splitting scheme where the measured damping rate (plain line) as a function of the time step integration, for a simulation with $\beta = 1\%$ is shown. The dashed line represents the numerical value, based on the solution of Eq. (3.2), which is found to be $\gamma^{(\mathrm{N})}/\omega_{ci} = -9.915 \times 10^{-4}$.

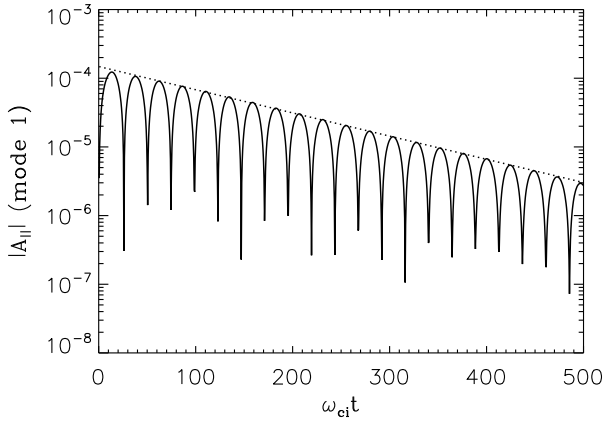

Figure 3: Time evolution of the norm of the parallel component of the vector potential for the same parameters as in Fig. 1. The slope of the dotted line is used as an estimate of the damping rate of the normal mode.

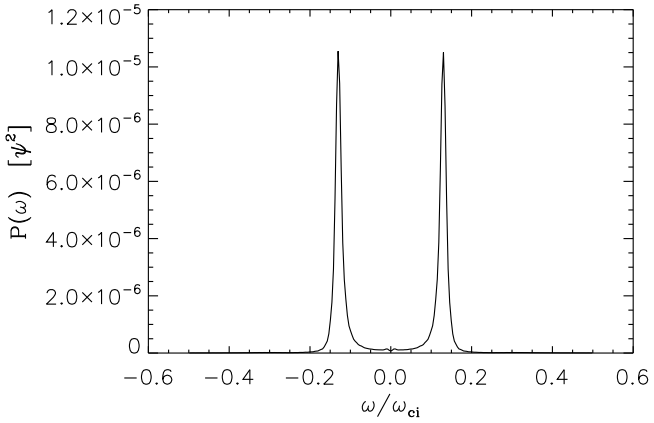

Figure 4: Power of spectrum of the generalized magnetic potential for a linear simulations of normal mode based on $N_t = 5000$ time steps. The exact real mode frequency is $\omega_r/\omega_{ci} = \pm 0.130$ is in excellent agreement with the computed real frequency $\omega_r/\omega_{ci} \pm 0.129$.

After having investigated the properties of the normal mode of the system for $\omega_\star = 0$ we study the case of electromagnetic drift waves and electromagnetic ITG modes. We first consider the case of electromagnetic drift waves, that is $\eta_i = \eta_e = 0$. We have carried out a linear simulation using $N_e = N_i = 28657$ markers on a grid of length $L = 16\rho_s$ and a time step of $\omega_{ci}\Delta t = 1.0$; the density scalelength parameter is taken as $\kappa_n \rho_s = 0.15$ and $\beta = 0.02\%$. The electromagnetic splitting scheme yields a mode frequency and a linear growth rate of $(\omega_r;\gamma)/\omega_{ci} = (5.14\times10^{-2};2.42\times10^{-3})$ in excellent agreement with the exact values, determined from the numerical solution of the complete dispersion relation Eq. (3.1), $(\omega_r^{(N)};\gamma^{(N)})/\omega_{ci} = (5.14\times10^{-2};2.46\times10^{-3})$. In contrast, using the same physical parameters and the same initial conditions, the conventional δf method yields $(\omega_r;\gamma)/\omega_{ci} = (4.95\times10^{-2};2.18\times10^{-3})$; although the real part of the mode frequency is

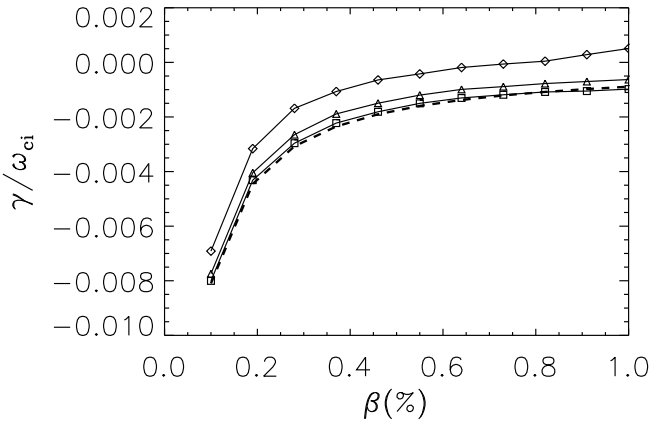

Figure 5: Damping rate of the kinetic shear-Alfvén wave as a function of β for various time steps of integration: $\omega_{ci}\Delta t=1$ (thin plain line with diamond symbols); $\omega_{ci}\Delta t=0.5$ (thin plain line with triangle symbols); and $\omega_{ci}\Delta t=0.1$ (thin plain line with square symbols). The thick dashed curves represents the numerical solution of the complete dispersion relation, Eq. (3.2). The number of markers is $N_e=N_i=46368$ and the total simulation time used in each case, during which the damping rate is evaluated, is the same: $\omega_{ci}T=500$.

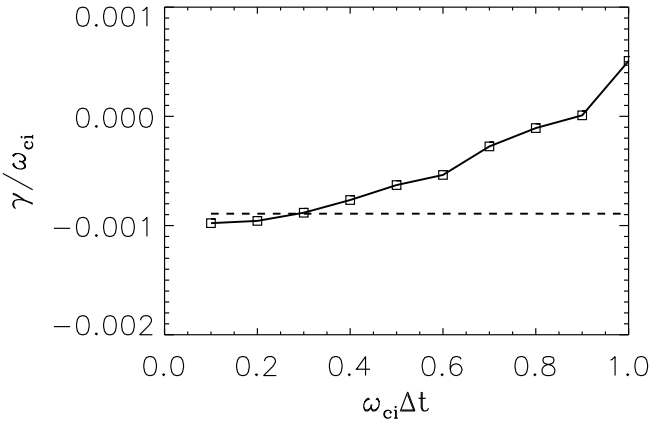

Figure 6: Damping rate of the kinetic shear-Alfvén wave as a function of the time step of integration. The damping rate based on the numerical solution of the dispersion relation (3.2) is $\gamma^{(\mathrm{N})}/\omega_{ci}=-8.915\times10^{-4}$. The total simulation time and the number of electron and ion markers are the same as in Fig. 4.

in reasonable agreement with the exact value, the measured growth rate departs quite significantly from the theoretical value. By varying the drive of the drift waves, i.e. by varying κ_n, we have systematically observed an accuracy problem with the δf scheme; a similar observation was also reported in the electrostatic case [26]. In order to understand the difference in accuracy between the conventional δf scheme and the electromagnetic splitting scheme, one can resort to the information contained in the power spectrum.

Fig. 7 shows the power spectrum for $|\psi|^2$ based on a linear simulation with $N_t=5000$ time steps, $\kappa_n\rho_s=0.1$ and $\beta=0.01\%$. The peak of the power spectrum is located around $\omega_r/\omega_{ci}=3.7\times10^{-2}$ in good agreement with the exact numerical value of $\omega_r^{(\mathrm{N})}/\omega_{ci}=3.5\times$

10^{-2}. However the power spectrum shows the appearance of high-frequency modes in the simulated plasma; it is interesting (but not surprising) to note that the high-frequency modes appear in the vicinity of the shear Alfvén frequency $\omega_{\rm A} = k_{\|} c_s / \sqrt{\beta}$ (using the simulation parameters mentioned above, the shear Alfvén frequency, $\omega_{\rm A} = k_{\|} c_s / \sqrt{\beta}$, is found to be $\omega_{\rm A}/\omega_{ci} \simeq 0.39$). Fig. 8 shows the power spectrum for $|\psi|^2$ based on a linear simulation using the electromagnetic splitting scheme; all the physical and simulation parameters, as well as the initial conditions, are the same as in Fig. 7. *The high-frequency noise is absent from the simulated plasma*. The reason for the high-frequency modes in the δf scheme is due to the fact that fast particles, $v_{\|} \sim \omega_A / k_{\|}$, introduce noise in the weight equation (see the $v_{\|}$ contribution in Eq. (2.6)) which is then fed into the field equations. The electromagnetic splitting scheme circumvents this problem by *analytically* removing the source of the 'noise contamination' by the fast particles, that is by removing the $v_{\|}$ term in the weight equation, Eq. (2.11). This is the reason for the significant differences between Figs. 7 and 8.

We continue our study of the linear properties of the electromagnetic splitting scheme by considering the finite-β ITG mode. In particular we study the transition between the ITG branch and the drift wave branch by varying the density scalelength parameter κ_n while keeping the ion temperature gradient parameter, κ_{T_i}, fixed; here $\kappa_{T_i}\rho_s = 0.1$. Fig. 9 shows the real part of the mode frequency for a linear simulation, using the electromagnetic splitting scheme, with $N_i = N_e = 46368$ markers and $\beta = 0.01\%$, as a function of the parameter κ_n. The thin plain line in Fig. 9 represents the numerical solution of the dispersion relation, Eq. (3.1), whereas the squares (connected through a dotted line) represents the computed value of ω_r. Note that as κ_n increases the ITG parameter η_i decreases. The right curve is the drift wave branch whereas the left curve, $\kappa_n \rho_s \lesssim 0.04$, represents the ITG branch. Fig. 10 shows the linear growth rate for the same set of simulations as in Fig. 9. Note that near the transition from the ITG branch to the drift wave branch, which occurs around $\kappa_n \rho_s \simeq 0.04$, the computed growth rate departs moderately from the theoretical value; the reason for the discrepancy is due to the fact that the linear growth rate is very small in this region. However the overall agreement between the computed and theoretical linear growth rates is excellent. As mentioned earlier, the efficient removal of the noise in the simulated plasma is a reason for the success of the electromagnetic splitting scheme. Another reason for the good agreement shown in Figs. 9 and 10 is also due to the fact that the number of markers per cell, $N_c \equiv N_e / N_g$ (recall N_g is the number of grid points in the simulation domain), used in these simulations is large; in Figs. 9 and 10, we have $N_c = 724$. Increasing N_c is equivalent to increase the resolution of the simulated plasma in phase space which, in turn, implies that the accuracy of the computed linear growth rate is improved (this is of course true for both the electromagnetic splitting scheme and the conventional δf scheme). However an increase in N_c implies an increase in the computational effort, denoted $W_{\rm comp}$.

For sufficiently large values of N_c we have $W_{\rm comp} \propto N_c$. Therefore it is important to select a value of N_c such as to achieve a phase space resolution to correctly model

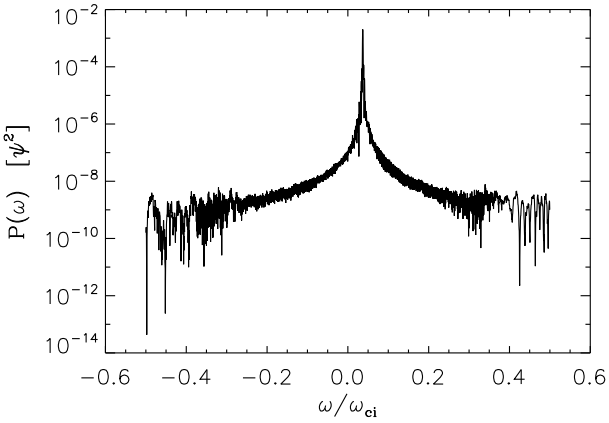

Figure 7: Power spectrum of $|\psi|^2$ for a linear simulation of electromagnetic drift waves using the standard δf scheme based on $N_t=5000$ time steps. Other parameters are: $\kappa_n\rho_s=0.1$, $\beta=0.01\%$ and $\omega_{ci}\Delta t=1.0$.

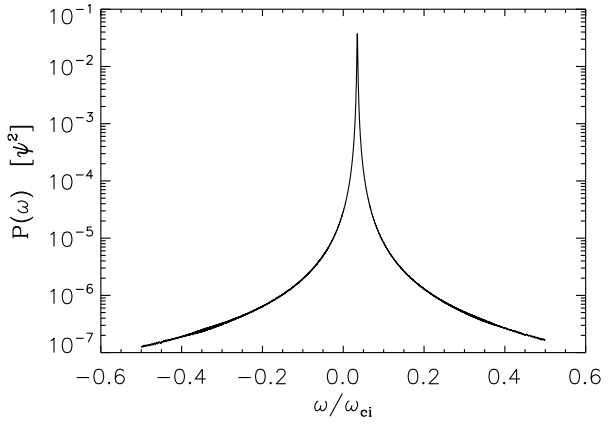

Figure 8: Power spectrum of $|\psi|^2$ for a linear simulation of electromagnetic drift waves using the electromagnetic splitting scheme based on $N_t=5000$ time steps. Other parameters are: $\kappa_n\rho_s=0.1$, $\beta=0.01\%$ and $\omega_{ci}\Delta t=1.0$.

the physics of interest, while at the same time to minimize the computational work. In order to understand the phase space resolution requirements, we have carried a set of linear simulations of electromagnetic drift waves by varying the parameters N_c while keeping other parameters fixed ($\kappa_n\rho_s=0.15$, $L=16\rho_s$, $N_g=64$, $\beta=0.05\%$, $N_t=2000$ and $\omega_{ci}\Delta t=1.0$). Note that the total number of electron markers has been taken equal to the total number of ion markers. Fig. 11 shows the linear growth rate of electromagnetic drift waves as a function of N_c. The thick dashed line shows the exact (numerical) value of the linear growth rate: $\gamma^{(\mathrm{N})}/\omega_{ci}=2.5\times10^{-3}$. The computed linear growth rates using the electromagnetic splitting scheme are shown as squares whereas the triangles are for the conventional δf scheme. As observed previously the splitting scheme is more accurate than the δf scheme. There are two important observations that can be made based on

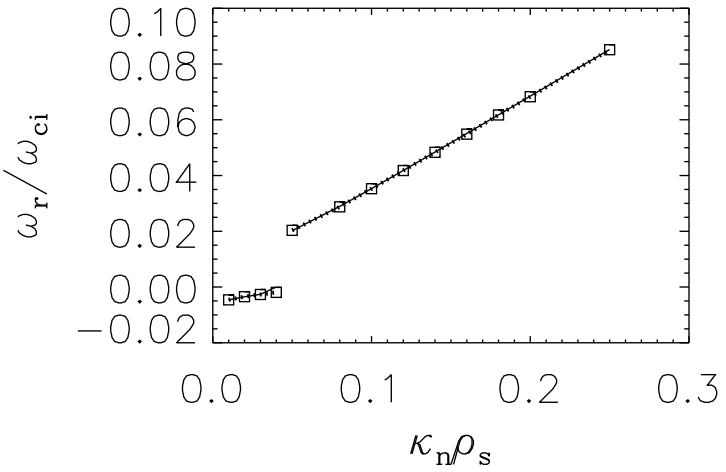

Figure 9: Real part of the mode frequency as a function of κ_n using the electromagnetic splitting scheme. The parameter η_i is varied such that the parameter κ_{T_i} is held fixed with $\kappa_{T_i}\rho_s = 0.1$. Other parameters are: $\omega_{ci}\Delta t = 1.0$, $L = 16\rho_s$ and $\beta = 10^{-4}$.

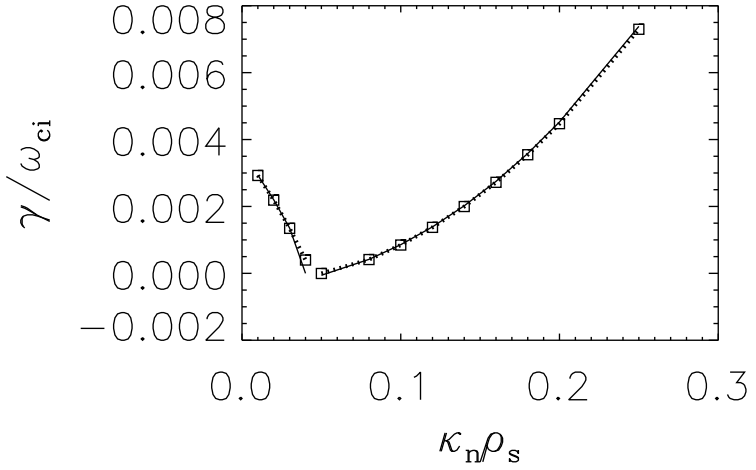

Figure 10: Linear growth rate as a function of κ_n using the electromagnetic splitting scheme. The parameter η_i is varied such that the parameter κ_{T_i} is held fixed with $\kappa_{T_i}\rho_s = 0.1$. Other parameters are: $\omega_{ci}\Delta t = 1.0$, $L = 16\rho_s$ and $\beta = 10^{-4}$.

Fig. 11. First, the number of markers per cell required to achieve a reasonably accurate linear growth rate is in the range $N_c \in [10,100]$ *both* for the splitting scheme and the δf scheme; however when the physical parameters suggest the presence of a robust linear growth rate, a smaller value of N_c can be used in the simulations. The second observation pertaining to Fig. 11 is regarding the asymptotic behavior of the computed linear growth rate.

It would seem plausible in the limit $N_c \mapsto \infty$ that the difference between the com-

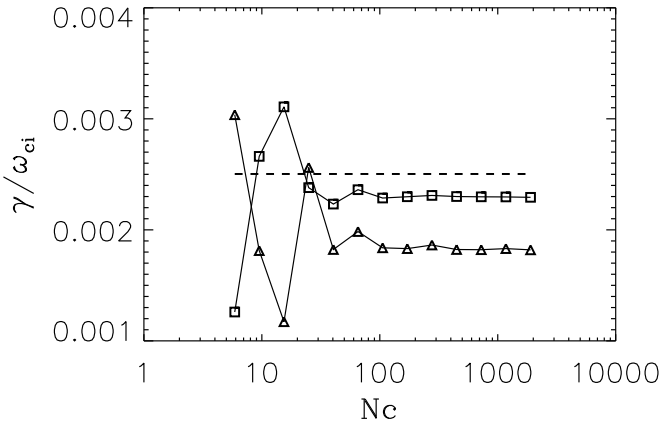

Figure 11: Linear growth rate as a function of the number of markers per cell, N_c, for linear electromagnetic drift wave simulations. The parameters used are: $\kappa_n\rho_s=0.15$, $N_g=64$, $N_t=2000$, $\omega_{ci}\Delta t=1.0$ and $\beta=0.05\%$.

puted growth rate and the theoretical growth rate would (almost) vanish, since the region of velocity space around $v_r\sim\omega_r/k_\parallel$ contains more markers as N_c increases. However the finite grid spacing and time step of integration do also affect the accuracy of the simulations. In our specific case (for the physical and simulation parameters of Fig. 11), the spatial resolution should not significantly affect the computed linear growth, since we have been considering the lowest-order mode number ($n=1$), i.e. we have $k_\perp\Delta x=(2\pi n/L)(L/N_g)=2\pi/N_g=\pi/32\ll 1$. However the time step of integration may have a more dramatic impact on the accuracy of the computed linear growth rate. To prove this point, a set of linear simulations for the same parameters as in Fig. 11, and for a fixed number of markers per cell of $N_c=105$, has been carried out by varying the time step of integration. For the sake of comparison, the total simulation time for each simulation is fixed to $\omega_{ci}T=2000$; therefore the number of time steps used varies according to $N_t=\mathcal{N}(T/\Delta t)$ where $\mathcal{N}(x)$ denotes the nearest integer to x.

Fig. 12 shows the computed linear growth rate as a function of the time step of integration; the dashed line shows the exact linear growth rate, $\gamma^{(\mathrm{N})}/\omega_{ci}=2.5036\times 10^{-3}$. A numerical instability occurs for $\omega_{ci}\Delta t\gtrsim 2.0$; as expected the computed linear growth rate satisfies the correct asymptotic behavior of

$$\lim_{\Delta t\mapsto 0}\left|\gamma-\gamma^{(\mathrm{N})}\right|=0.$$

In summary, the accuracy of the splitting scheme is related to its noise suppressing property. Specifically the noise contamination of the simulated plasma is almost inexistent. This can be traced back to the absence of $v_\parallel$ contribution in the weight equation, see, Eq. (2.11). In addition, as discussed in Section 5, the absence of terms involving the parallel velocity (of the electrons) in the weight equation is also crucial in achieving energy conservation (this is also true in the electrostatic version of the scheme [1]). The number of markers per cell also influence the accuracy of the scheme in the linear regime (this

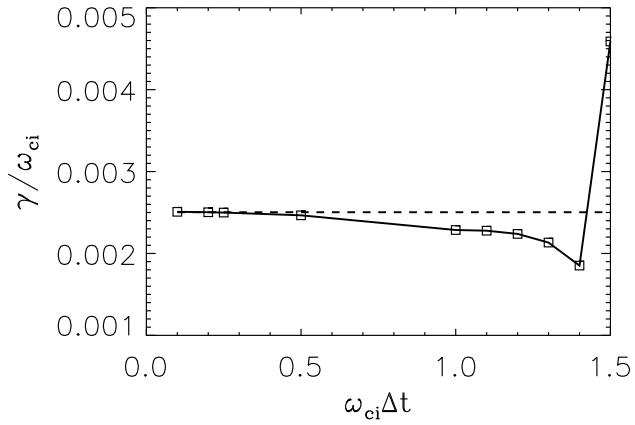

Figure 12: Linear growth rate as a function of the time step of integration for linear electromagnetic drift wave simulations. The parameters used are: $\kappa_n\rho_s=0.15$, $N_g=64$, $N_t=2000$, $N_c=N_e/N_g=105$ and $\beta=0.05\%$. The dashed line shows the exact (theoretical) value obtained from the numerical solution of the dispersion relation, Eq. (3.1).

is of course true for the δf scheme and other related numerical approaches). The appropriate number of markers per cell, N_c, depends on the magnitude of the linear growth rate, γ; the smaller γ the larger N_c and vice-versa. The time step of integration is also an important factor: although it is possible to marginally violate the CFL criterion [9], this occurs at the cost of the accuracy; for improved accuracy one must usually use a time step smaller than (or close to) $(\Delta t)_{\text{CFL}}$.

The simulation results presented so far were for low-β plasmas, i.e. $\beta m_i/m_e<1$. We have performed a linear simulation with $N_c=448$ markers per cell, $N_g=64$, $\omega_{ci}\Delta t=1.0$ and $\kappa_n\rho_s=0.1$. The plasma beta is $\beta=0.06\%$ which is slightly larger than the critical value $\beta_c=m_e/m_i$. The theoretical growth rate in this case is $\gamma^{(\text{N})}/\omega_{ci}=0.00098$. The measured growth rate is found to be $\gamma/\omega_{ci}=0.00034$: this is almost 3 times smaller than the theoretical value. If we increase β further we found that the measured linear growth rate becomes much larger than its theoretical value; smaller time steps and more markers per cell did not alleviate the problem. A further increase in β resulted in a numerical instability. This numerical instability is investigated in the next section.

4 Numerical dispersion relation

As it is has been mentioned in the previous section, a numerical instability appears to occur when β is of the order of (or larger than) the mass ratio, m_e/m_i. As it turns out increasing the resolution in configuration space (increasing the number of grid points, N_g) and in phase space (increasing the number of markers per cell, N_c) does not cure the problem. Therefore it is worth looking back at the field equations actually being solved in the splitting scheme and investigate their linear properties.

In order to explain the behavior of the simulated plasma around $\beta\sim m_e/m_i$ we con-

sider a simplified set of field equations by neglecting scalar nonlinearities of second order and higher as well as all collisional effects. The resulting set of field equations is given by

$$\left(\frac{\partial^2}{\partial y^2}-\eta\right)\Phi=\eta\mathsf{U}-\rho \tag{4.1}$$

$$\frac{\partial^2 A_\parallel}{\partial y^2}=-\beta J_\parallel\,, \tag{4.2}$$

$$\left(\frac{\partial^2}{\partial y^2}-\eta\right)E_\parallel=\nabla_\parallel\rho-\beta\nabla_{||}P+\beta\xi\kappa\frac{\partial A_\parallel}{\partial y}\,, \tag{4.3}$$

$$\frac{\partial^2\chi}{\partial y^2}=\beta\left(\nabla_\parallel P-\xi\kappa\frac{\partial A_\parallel}{\partial y}\right), \tag{4.4}$$

$$\left(\frac{\partial^2}{\partial y^2}-\beta/\epsilon\right)\varpi=\nabla_\parallel^2(\beta Q-J_\parallel)-\beta\xi\kappa\frac{\partial E_\parallel}{\partial y}\,, \tag{4.5}$$

where $\eta=1+1/\tau$ and $\kappa\equiv\kappa_n$ (this slight change of notation for κ_n is to prevent confusion with the Fourier mode representation; see below, Eq. (4.8)). In addition we have the usual relations of $\chi=\nabla_\parallel\mathsf{U}$, $\varpi=-\nabla_\parallel\varphi$ and $\varphi=\partial\psi/\partial t$. In Eqs. (4.1)-(4.5) we have introduced the following quantities

$$\begin{aligned}\rho&=\int_{-\infty}^{+\infty}(h_i-h_e)dv_\parallel\,,\quad J_\parallel=\int_{-\infty}^{+\infty}(h_i-h_e)v_\parallel dv_\parallel\,,\\ P&=\int_{-\infty}^{+\infty}(h_i-h_e)v_\parallel^2 dv_\parallel\,,\quad Q=\int_{-\infty}^{+\infty}(h_i-h_e)v_\parallel^3 dv_\parallel\,.\end{aligned} \tag{4.6}$$

The above expressions require to take the appropriate velocity moments of the nonadiabatic responses for both species. In contrast with the usual derivation of the linear dispersion relation (presented in Appendix B), the scalar field $\varphi=\partial\psi/\partial t$ is treated as an *independent* scalar field (that is on the same footing as Φ or $A_\parallel$) since this is the actual quantity used in the dynamical evolution of the non-adiabatic weight, Eq. (2.11). Substituting Eq. (2.10) in Eq. (2.1), neglecting collisional effects, assuming perturbations of the form $\exp(i\mathbf{k}\cdot\mathbf{x}-i\omega t)$, and linearizing, we obtain (in physical units)

$$h_j=\left(-i\omega+ik_\parallel v_\parallel\right)^{-1}\left[\theta_j\omega_{ci}\frac{e\varphi}{T_e}-i\omega_\star g_j\frac{e\phi}{T_e}\right]F_{Mj}\,, \tag{4.7}$$

where all the quantities have been defined in Appendix B. As just mentioned we treat φ in the above equation as an independent scalar field, rather than making the real space-to-Fourier space transformation of $\varphi\mapsto-i\omega\psi$, as done in Appendix B. The set of simplified equations (4.1)-(4.5) has no nonlinear terms; further the system being assumed to be periodic in the y direction with period L, it is convenient to write each fluctuating quantity, say Φ, as

$$\Phi(y,t)=\sum_n\Phi_n(t)e^{ik_0ny}\,, \tag{4.8}$$

where $k_0 \equiv 2\pi/L$. Similar Fourier representations are used for the scalar fields, $A_\parallel$, ϖ, $E_\parallel$, χ, and for the velocity moments, ρ, $J_\parallel$, P, Q, defined in Eq. (4.6). The velocity moment of the nonadiabatic response (4.7) of order k is found to be

$$N_j^{(k)} \equiv \int_{-\infty}^{+\infty} h_j v_\parallel^k dv_\parallel = -in_0 c_s^k \frac{(\sqrt{2}\alpha_j)^k}{\omega_{\parallel j}} \sum_{\ell=0}^{3} R_j^{(\ell)} Z^{(k+\ell)}(\zeta_j), \tag{4.9}$$

where $\alpha_j = \sqrt{(T_j m_i)/(T_e m_j)}$, $\omega_{\parallel j} = \sqrt{2} k_\parallel V_{\mathrm{th}j}$,

$$R_j^{(0)} = \theta_j \omega_{ci}(e\varphi/T_e) - i\omega_\star(1-\eta_j/2)(e\Phi/T_e), \quad R_j^{(1)} = i\omega_\star(1-\eta_j/2)\sqrt{2}\alpha_j(A_\parallel/(\rho_s B_0)),$$
$$R_j^{(2)} = -i\omega_\star\eta_j(e\Phi/T_e), \quad R_j^{(3)} = i\omega_\star\eta_j\sqrt{2}\alpha_j(A_\parallel/(\rho_s B_0)),$$

and

$$Z^{(k)}(\zeta) \equiv \frac{1}{\sqrt{\pi}} \int_{-\infty}^{+\infty} \frac{x^k}{x-\zeta} e^{-x^2} dx,$$

for non-negative integer k and complex ζ. The required amplitudes $(\Phi_n, A_{\parallel n}, \varphi_n)$ can be obtained by writing Eqs. (4.1)-(4.5) in Fourier space; this procedure yields

$$\begin{pmatrix} \Phi_n \\ A_{\parallel n} \\ \varphi_n \end{pmatrix} = \mathbf{M} \begin{pmatrix} \rho_n \\ J_{\parallel n} \\ P_n \\ Q_n \end{pmatrix} \equiv \begin{pmatrix} r_1 & r_2 & r_3 & 0 \\ 0 & \beta/k_\perp^2 & 0 & 0 \\ s_1 & s_2 & s_3 & s_4 \end{pmatrix} \begin{pmatrix} \rho_n \\ J_{\parallel n} \\ P_n \\ Q_n \end{pmatrix}, \tag{4.10}$$

where

$$r_1 = 1/(k_\perp^2+\eta), \quad r_2 = -\beta^2\eta\xi\kappa/(\theta k_\perp^4(k_\perp^2+\eta)), \quad r_3 = \beta\eta/(k_\perp^2(k_\perp^2+\eta)),$$
$$s_1 = i\xi_2/k_\perp, \quad s_2 = i\xi_3/(\theta k_\perp), \quad s_3 = -i\beta\xi_2/k_\perp, \quad s_4 = i\beta\xi_1/(\theta k_\perp),$$
$$\xi_1 = \frac{\theta^2 k_\perp^2}{k_\perp^2+\beta/\epsilon}, \quad \xi_2 = \frac{\beta\xi\kappa k_\perp^2}{(k_\perp^2+\eta)(k_\perp^2+\beta/\epsilon)}, \quad \xi_3 = \frac{\beta^3\xi^2\kappa^2 - \theta^2 k_\perp^2(k_\perp^2+\eta)}{(k_\perp^2+\eta)(k_\perp^2+\beta/\epsilon)}.$$

We must now determine the linear response of the velocity moments in Eq. (4.6) in terms of the perturbed scalar fields Φ, $A_\parallel$ and φ. Using the expression for the velocity moments of the nonadiabatic response, Eq. (4.9), one gets

$$\begin{pmatrix} \rho_n \\ J_{\parallel n} \\ P_n \\ Q_n \end{pmatrix} = -i\mathbf{Q} \begin{pmatrix} \Phi_n \\ A_{\parallel n} \\ \varphi_n \end{pmatrix} \equiv -i \begin{pmatrix} a_0 & b_0 & c_0 \\ a_1 & b_1 & c_1 \\ a_2 & b_2 & c_2 \\ a_3 & b_3 & c_3 \end{pmatrix} \begin{pmatrix} \Phi_n \\ A_{\parallel n} \\ \varphi_n \end{pmatrix}, \tag{4.11}$$

where

$$a_k = \sum_j (\sqrt{2}\alpha_j)^k Z_j \alpha_j^{(k)}, \quad b_k = \sum_j (\sqrt{2}\alpha_j)^k Z_j \beta_j^{(k)}, \quad c_k = \sum_j (\sqrt{2}\alpha_j)^k Z_j \mu_j^{(k)},$$

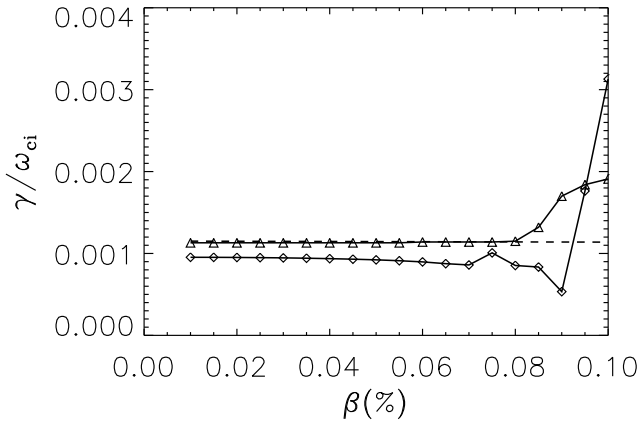

Figure 13: Linear growth rate as a function of β for electromagnetic drift waves with $\kappa_n\rho_s=0.1$, $N_c=448$ markers per cell, $N_g=64$, $\omega_{ci}\Delta t=1.0$ and $k_\perp\rho_s=0.39$. The thick dashed line is the exact expression for the linear growth rate, the plain line with diamond symbols represent the growth rate as measured from the linear simulations and the plain line with triangle symbols represents the solution of the 'numerical dispersion relation', Eq. (4.12).

(for $k=1,2,3$); in addition the following definitions have been used:

$$\alpha_j^{(k)}=\theta_j\frac{\omega_{ci}}{\omega_{\|j}}\,Z^{(k)}(\zeta_j),\quad \beta_j^{(k)}=-i\frac{\omega_\star}{\omega_{\|j}}\,S^{(k)}(\zeta_j),\quad \mu_j^{(k)}=i\frac{\omega_\star}{\omega_{\|j}}\,\sqrt{2}\alpha_j S^{(k+1)}(\zeta_j),$$

and

$$S^{(k)}(\zeta_j)\equiv\left[1+\eta_j(\zeta_j^2-1/2)\right]Z^{(k)}(\zeta_j)+\eta_j\left[I_{k+1}+\zeta_j I_k\right],$$

where the definition of I_k for non-negative integer k is given in Appendix B. Combining Eqs. (4.10) and (4.11) the *numerical* dispersion relation based on the electromagnetic splitting scheme is

$$\mathcal{D}_{\rm NUM}(\omega;\mathbf{k})\equiv\det\left(\mathbf{I}+i\mathbf{QM}\right)=0, \tag{4.12}$$

where $\mathbf{I}$ is the identity matrix, and the matrices $\mathbf{M}$ and $\mathbf{Q}$ are defined in Eqs. (4.10) and (4.11), respectively. Since both the dispersion relation, Eq. (3.1), and the numerical dispersion relation, Eq. (4.12), are based on linearized equations they should be equivalent. For $\beta\ll m_e/m_i$ the numerical solution of Eqs. (3.1) and (4.12) do, in fact, agree exactly (within round-off errors) over many decades in β (specifically $\beta\in[10^{-12},10^{-4}]$). However the numerical solution of the numerical dispersion relation (4.12) reveals the presence of a spurious mode with a substantial growth rate for $\beta\gtrsim m_e/m_i$. This is shown as a plain line with triangles in Fig. 13 (for a linear simulation with $\kappa_n\rho_s=0.1$, $\omega_{ci}\Delta t=1.0$, $k_\perp\rho_s=0.39$ and $N_c=448$ markers per cell). The computed linear growth rate using the splitting scheme is shown as a plain line with diamond symbols. The dashed line represents the linear growth determined from the dispersion relation (3.1); the linear growth rate decreases approximately linearly with β for small β:

$$\gamma \approx (1-\beta\Omega_0^2)\frac{\sqrt{\pi}\zeta_0}{1+b}\left[\omega_\star(1-\eta_e/2)-\omega_{r0}\right], \tag{4.13}$$

where $\zeta_0=\omega_{r0}/(\sqrt{2}k_{||}V_{the})$, $\omega_{r0}=\omega_\star/(1+b)$, $\Omega_0=\omega_{r0}/(k_{||}c_s)$ and $b=k_\perp^2\rho_s^2$. Fig. 13 indicates that a spurious mode is present in the simulation. However, given the complexity of the numerical dispersion relation, Eq. (4.12), the origin of the numerical instability remains unclear. Recall that for $\omega_\star\equiv 0$, the electromagnetic splitting scheme is not only numerically stable but also very accurate even for $\beta \gg m_e/m_i$ (see, for example, Fig. 5). This suggests that the origin of the numerical instability can presumably be related to the drive due to the density gradient. To show this, let us Fourier transform Eqs. (4.2), (4.3) and (4.5), *except the term involving the parallel gradient* (for reasons that will become clear below)

$$(k_y^2+\eta)E_{\|n}=\nabla_\|(\beta P_n-\rho_n)-ik_y\beta\xi\kappa A_{\|n}, \tag{4.14}$$

$$k_y^2 A_{\|n}=\beta J_{\|n}, \tag{4.15}$$

and

$$(k_y^2+\beta/\epsilon)\varpi_n=\nabla_\|^2(J_{\|n}-\beta Q_n)+ik_y\beta\xi\kappa E_{\|n}, \tag{4.16}$$

where $k_y\equiv nk_0$. Using Eqs. (4.14) and (4.15) in Eq. (4.16) one gets

$$\varpi_n=\frac{1}{k_y^2+\beta/\epsilon}\,\nabla_\|^2(J_{\|n}-\beta Q_n)+c_2J_{\|n}-ic_1\nabla_\|(\beta P_n-\rho_n), \tag{4.17}$$

where

$$c_1=-\beta\xi\kappa\frac{k_y}{(k_y^2+\beta/\epsilon)(k_y^2+\eta)}\ , \quad c_2=\frac{\beta^3\xi^2\kappa^2}{(k_y^2+\beta/\epsilon)(k_y^2+\eta)}\ .$$

Upon inspection of Eq. (4.17), the numerical instability for finite $\omega_\star$ arises from the *odd* velocity moments, that is from the current density and the heat flux density. Specifically, using the real space to Fourier space transformation of $\nabla_\| \mapsto i\theta k_y$ in Eq. (4.17) for the current density only one finds

$$\varpi_n=-\alpha J_{\|n}-\frac{\beta}{k_y^2+\beta/\epsilon}\,\nabla_\|^2 Q_n-ic_1\nabla_\|(\beta P_n-\rho_n), \tag{4.18}$$

where

$$\alpha\equiv\frac{1}{k_y^2+\widehat{\beta}}\left[\theta^2k_y^2-\frac{\epsilon\widehat{\beta}^3\kappa^2(1+\eta_e)^2}{k_y^2+\eta}\right], \tag{4.19}$$

and $\widehat{\beta} \equiv \beta/\epsilon$. The source of the numerical instability is now evident. For small β the factor multiplying the current density is positive; as β increases the value of α decreases and ultimately becomes negative. A negative coefficient α is equivalent to a negative diffusion coefficient in a (linear) diffusion equation: there is no bounded solutions to such equations. Of course there are other terms on the right-hand side of Eq. (4.18) that may partially mitigate the effect of a negative coefficient α. The critical β for the numerical stability of the electromagnetic splitting scheme is obtained by solving $\alpha(\beta_c) = 0$ which yields

$$\beta_c = \left(\frac{\theta \epsilon k_y}{\kappa(1+\eta_e)} \right)^{2/3} (k_y^2 + 1 + 1/\tau)^{1/3}. \tag{4.20}$$

For the simulation parameters of Fig. 13, one finds that $\beta_c = 9.95 \times 10^{-4}$, in excellent agreement with the threshold of the numerical instability observed in the actual simulations. It is not clear if it is possible to avoid this numerical instability; more work is required to settle this issue.

5 Nonlinear electromagnetic simulations

In this section we present nonlinear simulations of electromagnetic drift waves in the collisionless case (Section 5.1) and in the presence of collisions (Section 5.2).

5.1 Collisionless nonlinear simulations

Fig. 14 shows the nonlinear time evolution of the lowest-order mode ($n=1$) for the generalized magnetic potential ψ. All the modes are retained in this simulation and are allowed to evolve freely (no smoothing of high-n modes is carried out). The simulation parameters are: $N_c = 105$, $\omega_{ci}\Delta t = 1.0$, $\kappa_n \rho_s = 0.1$ and $\beta = 0.01\%$. Since the linear growth rate for the $n=1$ mode is of the order of $\gamma_\ell/\omega_{ci} \sim 10^{-3}$ nonlinear effects will become important for $t \gtrsim 1/\gamma_\ell \approx 10^3 \omega_{ci}^{-1}$; this effect is clearly visible in Fig. 14. Ultimately the $n=1$ mode (and all other modes present in the system) saturates.

Fig. 15 shows the Fourier spectrum of the electrostatic potential for a nonlinear electromagnetic simulation using the splitting scheme in the fully saturated state ($\omega_{ci} T = 5000$). The simulation parameters used are: $N_g = 256$, $\theta = 10^{-2}$, $\kappa_n \rho_s = 0.1$, $\omega_{ci}\Delta t = 1.0$, $N_i = N_e = 6765$ and $\beta = 0.01\%$. The χ^2 fit, shown as a thin plain line in Fig. 15, indicates that the Fourier spectrum for the electrostatic potential follows a power law $|\Phi_k| \sim k^{-2.36}$. Fig. 16 shows the Fourier spectrum for the parallel component of the vector potential, $A_\parallel$, for the same simulation as in Fig. 15. The χ^2 fit shows that $|A_{\parallel k}| \sim k^{-2.40}$. Interestingly, the exponent α in $|A_{\parallel k}| \sim k^{-\alpha}$ is weakly dependent on the plasma β at least for $\beta m_i/m_e < 1$. For instance, one finds that $\alpha = 2.30$ for $\beta = 0.02\%$ and $\alpha = 2.31$ for $\beta = 0.04\%$; the very weak dependence of α on the plasma β is not explained.

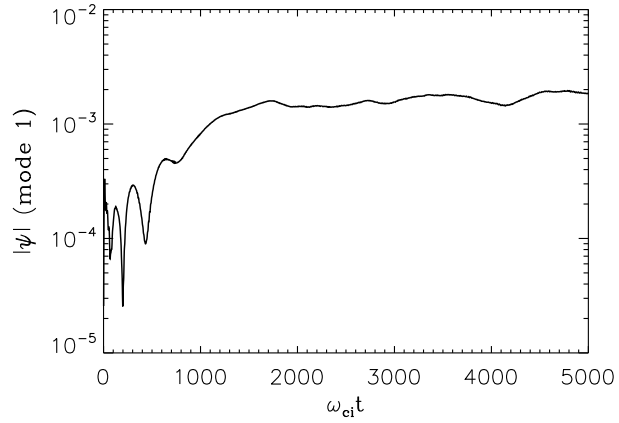

Figure 14: Nonlinear simulations of electromagnetic drift waves using the splitting scheme. The amplitude of the $n=1$ ψ mode as a function of time is shown. The physical and simulation parameters are: $N_c=105$, $\omega_{ci}\Delta t=1.0$, $\kappa_n\rho_s=0.1$ and $\beta=0.01\%$.

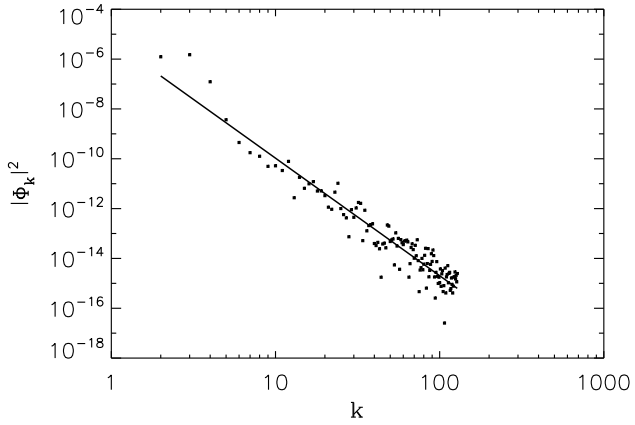

Figure 15: Spectrum of the electrostatic potential as a function of the mode number at the end $(\omega_{ci}T=5000)$ of a nonlinear simulation with 6765 markers. The physical and simulation parameters are: $N_g=256$, $\theta=10^{-2}$, $\kappa_n\rho_s=0.1$, $\omega_{ci}\Delta t=1.0$ and $\beta=0.01\%$. The χ^2 fit (shown as a plain line) yields $|\Phi_k|\sim k^{-2.36}$.

We now address the question of energy conservation. As shown in Appendix C, in the absence of collisions, the total energy E must be conserved:

$$E(t)=K(t)+U(t)+U_{\rm M}(t)=E(0)\,. \tag{5.1}$$

Here K, U and $U_{\rm M}$, defined as

$$K\equiv\sum_j\frac{m_j}{2}\int {v_{||}}^2F_jdv_{||}d^3x,\quad U\equiv\frac{e^2n_0{\rho_s}^2}{2T_e}\int|\boldsymbol{\nabla}_\perp\Phi|^2d^3x,\quad U_{\rm M}\equiv\frac{1}{8\pi}\int\left|\boldsymbol{\nabla}_\perp A_{||}\right|^2d^3x,$$

represent the volume averaged total kinetic energy, electrostatic potential energy and magnetic potential energy, respectively. As it was shown in the previous section, the

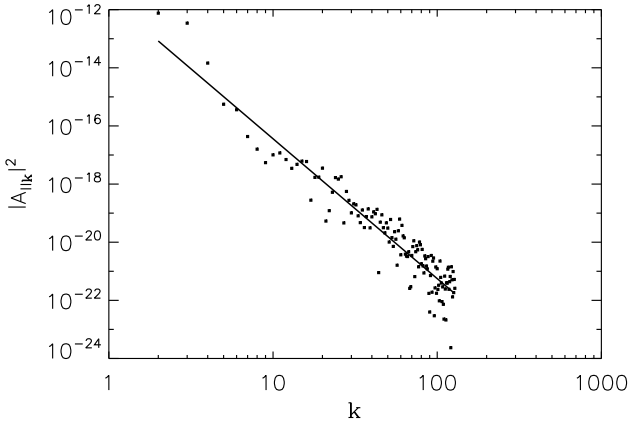

Figure 16: Spectrum of the parallel component of the vector potential as a function of the mode number for the same simulation as in Fig. 15. The χ^2 fit (shown as a plain line) yields $|A_{\|k}| \sim k^{-2.40}$.

splitting scheme is more accurate than the δf scheme as far as the linear properties (real mode frequency and growth rate) of the simulated plasma are concerned. However the significant advantage of the splitting scheme over the conventional δf scheme is its *nonlinear* properties. The energy conservation (or lack of) is a meaningful test in assessing the performance of a given numerical scheme and its correct implementation. Fig. 17 shows the time evolution of the total energy variation, $E(t)-E(0)$, as a function of time for nonlinear, collisionless simulations; the parameters are: $N_c = 10$ (number of markers per cell), $N_g = 64$, $\omega_{ci}\Delta t = 1.0$, $\kappa_n = 0.1$ and $\beta = 0.01\%$. The dotted line is the time evolution of $E(t)-E(0)$ obtained using the splitting scheme whereas the plain line is the same quantity based on the conventional δf scheme; the initial conditions in phase space for both runs are identical. In order to achieve perfect energy conservation one would need an infinite number of markers per cell and an infinitesimally small time step. However the time evolution of the total energy for the splitting scheme does not display a secular growth as for the case of the δf scheme. We believe that this is an important feature of the splitting scheme.

5.2 Nonlinear simulations with collisional effects

All simulations reported up to this point were carried out in the collisionless regime. In this section, we study the impact of collisional effects on electromagnetic drift modes. For simplicity we neglect collisional effects on the ion dynamics. The collision operator for the electron distribution function F_e is taken to be of the form

$$C(F_e) = \nu_{\rm ei}\left[V_{\rm the}^2\frac{\partial^2 F_e}{\partial v_\|^2} + \frac{\partial}{\partial v_\|}\left(v_\| F_e\right)\right], \tag{5.2}$$

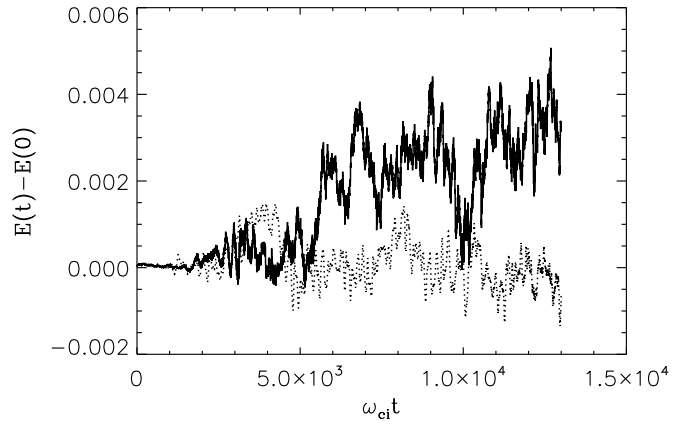

Figure 17: Total energy variation, $E(t)-E(0)$, as a function of time for a nonlinear simulations of electromagnetic drift waves with $\kappa_n\rho_s=0.1$, $\beta=0.01\%$, $N_c=10$ and $\omega_{ci}\Delta t=1.0$. The plain line is for the splitting scheme whereas the dotted line is for the conventional δf scheme (the same initial conditions in phase space were used for both simulations).

where the basic collision frequency ν_{ei} is taken to be constant and $V_{\rm the}=\sqrt{T_e/m_e}$ is the electron thermal velocity. The first term on the right-hand side represents the diffusive component in velocity space whereas the second contribution is due to the drag term. We note that the collision operator (5.2) satisfies the minimum requirements mentioned in Section 2, that is: it annihilates a Maxwellian distribution function; and that it conserves particle number

$$C(F_{Me})=\int_{-\infty}^{+\infty}C(F_e)dv_{\|}=0.$$

Note that collisional effects do influence the scalar fields that enter the formulation of the electromagnetic splitting scheme. In particular the equations governing $E_{||}$, Eq. (2.14), and ϖ, Eq. (2.16), depend on the velocity moments of the collision term. Using Eq. (5.2) the relevant quantities are (in normalized gyrokinetic units)

$$\begin{aligned}\sum_j Z_j C_j^{(1)}&=\nu_{\rm ei}\int_{-\infty}^{+\infty}h_e v_{\|}dv_{\|},\\ \sum_j Z_j C_j^{(2)}&=2\nu_{\rm ei}\left[\int_{-\infty}^{+\infty}h_e v_{\|}^2dv_{\|}-\epsilon^{-1}\int_{-\infty}^{+\infty}h_e dv_{\|}\right].\end{aligned}\tag{5.3}$$

Note that only the nonadiabatic response enters the above equations: this is a quite general result. To show this, we operate with the collision operator on the distribution function written in the form of $F_j=F_{Mj}e^{-q_j\psi/T_j}+h_j$ to obtain

$$C(F_j)=C\left(F_{Mj}e^{-q_j\psi/T_j}\right)+C(h_j)=e^{-q_j\psi/T_j}C(F_{Mj})+C(h_j)=C(h_j),$$

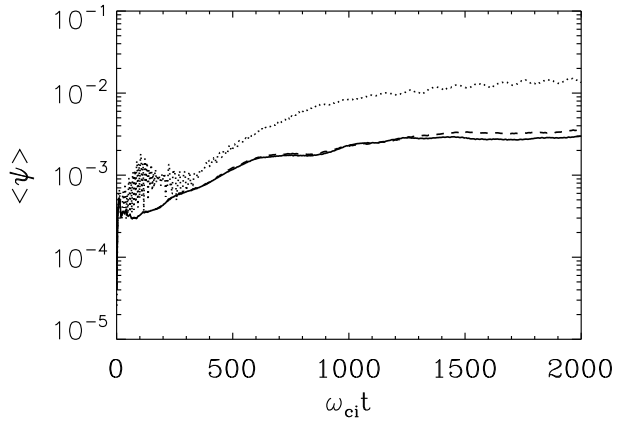

Figure 18: Time evolution of $\langle\psi\rangle$, as defined in Eq. (5.4), for a nonlinear simulations of collisional electromagnetic drift waves with $N_i=N_e=6765$ markers, $N_g=256$, $\omega_{ci}\Delta t=1.0$ and $\beta=0.01\%$.

where we have exploited the fact that the collision operator is linear and that it annihilates a Maxwellian distribution. We have carried out nonlinear simulations using the electromagnetic splitting scheme for various collision frequencies. The implementation of the collision operator (5.2) is based on the conventional approach of operator splitting [12,25]: in the first step, one integrates the *collisionless* orbits for each marker; in the second step, the scattering in velocity space, according to Eq. (5.2), is accounted for. Although this method is easy to implement, it is also noisy and possibly inaccurate (alternatively one can use a gridless, low-noise method for implementing the collisional effects [13] in PIC simulations). We expect the collision frequency to influence the turbulence level in the fully nonlinear regime. Since all the modes are retained in nonlinear simulations it is not meaningful to study the saturation of a single mode. Therefore we prefer to monitor the time evolution of

$$\langle\psi\rangle(t)\equiv\left(\frac{1}{L}\int_0^L\psi^2(y',t)dy'\right)^{1/2}. \tag{5.4}$$

Fig. 18 shows the time evolution of $\langle\psi\rangle$ for a nonlinear simulation of collisional electromagnetic drift waves with $N_i=N_e=6765$ markers, $N_g=256$, $\kappa_n\rho_s=0.1$ and $\omega_{ci}\Delta t=1.0$. The plain line is for the collisionless case, the dashed line is for $\nu_{\rm ei}/\omega_{ci}=10^{-2}$ whereas the dotted line is for $\nu_{\rm ei}/\omega_{ci}=10^{-1}$. Note that when the plasma is highly collisional, $\nu_{\rm ei}/\omega_{ci}=10^{-1}$, the quantity $\langle\psi\rangle$ does not saturate. To understand this, we substitute $F_e=F_{Me}+\delta f_e$ in Eq. (2.1)

$$\left(\frac{\partial}{\partial t}+v_\parallel\nabla_\parallel\right)\delta f_e-\frac{e}{m_e}E_\parallel\frac{\partial\delta f_e}{\partial v_\parallel}=C(F_{Me})-\widehat{L}_e(F_{Me}), \tag{5.5}$$

where the definitions of Eq. (2.3) have been used. The last term on the right-hand side of Eq. (5.5) represents the (linear) drive from the free energy stored in the electron pressure gradient. The only nonlinear term in the above equation is the last term on the

left-hand side of Eq. (5.5) which accounts for trapping of markers, with a characteristic frequency denoted ω_t, in the generalized magnetic potential ψ: in this simple one-dimensional model, this is the only source of nonlinearity that contributes to the saturation of the turbulence. We now consider the impact of the collision term on the saturation level of the turbulence. As the collision frequency is increased the electron markers that were originally trapped in the ψ potential (last term on the left hand-side of Eq. (5.5)) become progressively untrapped; ultimately when the collision frequency is sufficiently large, $\nu_{ei} \gtrsim \omega_t$, the turbulence cannot saturate and $\langle\psi\rangle$ keeps on growing. In a real three-dimensional system the cross-field electromagnetic nonlinearities would also contribute to the saturation of the turbulence.

6 Conclusions

We have presented the electromagnetic splitting scheme suitable for PIC simulations of microturbulence in the presence of kinetic electrons. It has been found that the electromagnetic splitting scheme allows for noise-free simulations of drift waves and ITG modes with fully kinetic electrons; in comparison the conventional δf scheme for the electron dynamics does not perform well, partly due to the fact that noise residing outside the normal modes of the system feeds back into the weight equation.

The present work has been carried out in a simple one-dimensional configuration; all contributions involving the $\mathbf{E}\times\mathbf{B}$ nonlinearity and the nonlinearity arising due to the magnetic flutter, $\boldsymbol{\mathcal{M}} = \boldsymbol{\nabla} A_{\parallel} \times \mathbf{B}_0 / B_0^2$, are absent in this simple model. The generalization of the electromagnetic splitting scheme to simulate plasma microturbulence in realistic fusion machines (e.g. tokamaks and stellarators) would require considerable efforts. Let us attempt to estimate the computational cost to include kinetic electron dynamics using the present scheme in a global, toroidal PIC code for the simulation of microturbulence. Specifically let us compare the computing requirements of a 3D simulation of ITG modes with adiabatic electrons with that of an equivalent simulation with fully kinetic electrons in the electromagnetic regime using the splitting scheme. Most computational work comes from the solution of global elliptic equations ('field solve') and from the time advance of markers in phase space ('particle pushing'). For simplicity we shall assume that the turbulence is quasi two-dimensional (in the plane perpendicular to $\mathbf{B}_0$); the elliptic equations can then be solved on a set of poloidal planes. Based on the electromagnetic splitting scheme one must resolve the magnetic skin depth, $\lambda_s = \rho_s / \widehat{\beta}$ and $\widehat{\beta} \equiv \sqrt{\beta m_i / m_e}$ [this requirement arises from the very nature of the elliptic equations to be solved (see Eq. (2.26) and following discussion)]. However in most situations it is sufficient to resolve the λ_s scale only radially while a ρ_s poloidally is appropriate. Therefore the number of grid points per poloidal plane required is of the order of $N_g^{(\beta)} \sim \pi a^2 / (\rho_s \lambda_s)$, where a is the minor radius of the plasma (here the superscript 'β' refers to the electromagnetic simulation). The corresponding number of grid points for the electrostatic case is $N_g \sim \pi a^2 / \rho_s^2$. The number of global elliptic equations to be solved for the electromagnetic case with

fully kinetic electrons is $N_f^{(\beta)}=5$; there is only one ($N_f=1$) such global elliptic equation to be solved for the case of an electrostatic simulation with adiabatic electrons. Assuming that one uses a near-optimal solver for the solution of each elliptic equation, the computational work for the field solve is proportional to $N_f N_g$; noting that $N_g^{(\beta)}/N_g \sim \rho_s/\lambda_s = \widehat{\beta}$ it follows

$$\frac{N_f^{(\beta)} N_g^{(\beta)}}{N_f N_g} \sim 5\widehat{\beta}.$$

We conclude that the computational cost of the field solve in the electromagnetic case is approximately $5\widehat{\beta}$ times larger than that for the electrostatic case with adiabatic electrons. For a plasma with $\beta=5\%$, we find that the above ratio is approximately 48. The computational cost for the 'particle pushing' scales approximately linearly with the number of markers in the simulation; note that the relevant parameter as far as phase space resolution is concerned is the number of markers per cell, N_c, rather than the total number of markers in the simulated plasma. Therefore the computational cost for particle pushing is proportional to $N_s N_c N_g$ where N_s is the number of species in the simulation. Assuming that the time step of integration for the electrostatic and electromagnetic simulations do not differ too much (a very *optimistic* approximation) and that N_c in both simulations is comparable, we find that

$$\frac{N_s^{(\beta)} N_c^{(\beta)} N_g^{(\beta)}}{N_s N_c N_g} \sim 2\widehat{\beta}.$$

For $\beta=5\%$ the above ratio is about 19. In summary, the overall computational cost can be estimated according to

$$W_{\text{comp}} \sim C_1 N_p N_f N_g + C_2 N_p N_s N_c N_g + C_3,$$

where N_f is the number of global elliptic equations to be solved, N_g is the number of grid points per poloidal plane, N_p is the number of poloidal planes in the simulation, N_c is the number of markers per cell for a given species and N_s is the number of species, C_1,C_2 and C_3 are constants. We conclude that a generalization of the electromagnetic splitting scheme to toroidal geometry is computationally prohibitive but may be within reach of massively-parallel supercomputers in the near future.

As mentioned earlier the generalization of the electromagnetic splitting scheme to simulate plasma microturbulence in realistic fusion machines (e.g. tokamaks and stellarators) would require considerable efforts. There are three obvious stumbling blocks to generalize the electromagnetic splitting scheme to fully three-dimensional, toroidal plasmas. First, as just discussed, the computational cost is prohibitive. The second stumbling block of the present version of the scheme is that it displays a cancelation problem which, if not addressed properly, generates a numerical instability. In order to bypass this numerical instability one can write the distribution function as $F_j = e^{-q_j\Phi/T_j} F_{Mj} + \widehat{h}_j$ (this is

essentially the *electrostatic* version of the splitting scheme [26]) where the response, $\widehat{h}_j$, does contain an adiabatic part which is not resolved explicitly. Such an approach will not be as accurate both linearly and nonlinearly as the electromagnetic splitting scheme but it is numerically easier to implement. Finally, even if one can solve all the required elliptic equations accurately, the intermediate quantities φ and ψ (given by Eq. (2.15) and Eq. (2.19), respectively) are determined from an integration along the equilibrium magnetic field line; to carry out such an integration *accurately and efficiently* in a toroidal system is far from obvious.

A Derivation of the field equations for the electromagnetic splitting scheme

The derivation of the field equations used in the electromagnetic splitting scheme requires the evolution equations of the first few velocity moments for the distribution functions of both species. Multiply

$$\left(\frac{\partial}{\partial t}+\mathbf{v}_E\cdot\boldsymbol{\nabla}\right)F_j+v_\parallel\widehat{\mathbf{b}}\cdot\boldsymbol{\nabla}F_j+\frac{q_j}{m_j}E_\parallel\frac{\partial F_j}{\partial v_\parallel}=C_j(F_j), \tag{A.1}$$

by $v_\parallel^k$, where k is a positive integer, and integrate over velocity space

$$\left(\frac{\partial}{\partial t}+\mathbf{v}_E\cdot\boldsymbol{\nabla}\right)\mathcal{M}_j^{(k)}+\widehat{\mathbf{b}}\cdot\boldsymbol{\nabla}\mathcal{M}_j^{(k+1)}-kE_\parallel\frac{q_j}{m_j}\mathcal{M}_j^{(k-1)}=C_j^{(k)}, \tag{A.2}$$

where

$$\mathcal{M}_j^{(k)}\equiv\int_{-\infty}^{+\infty}F_jv_\parallel^k dv_\parallel, \tag{A.3}$$

and

$$C_j^{(k)}\equiv\int_{-\infty}^{+\infty}C_j(F_j)v_\parallel^k dv_\parallel. \tag{A.4}$$

Writing $F_j=F_{Mj}+\delta f_j$, where F_{Mj} is a Maxwellian distribution with density n_0 and temperature T_j, we note that Eq. (A.3) can be written as

$$\mathcal{M}_j^{(k)}=n_0(\sqrt{2}V_{\mathrm{th}j})^kI_k+M_j^{(k)},$$

where $V_{\mathrm{th}j}=\sqrt{T_j/m_j}$,

$$I_k\equiv\frac{1}{\sqrt{\pi}}\int_{-\infty}^{+\infty}x^ke^{-x^2}dx,$$

and

$$M_j^{(k)} \equiv \int_{-\infty}^{+\infty} \delta f_j v_\parallel^k dv_\parallel \,, \tag{A.5}$$

is the k^{th} velocity moments of the perturbed distribution function. Multiplying Eq. (A.2) for $k=0$ with q_j and summing over species yields an equation for the charge number density $\rho \equiv \sum_j q_j \mathcal{M}_j^{(0)}$

$$\left(\frac{\partial}{\partial t} + \mathbf{V}_E \cdot \boldsymbol{\nabla}\right)\rho + \widehat{\mathbf{b}} \cdot \boldsymbol{\nabla} J_\parallel = \sum_j q_j C_j^{(0)} = 0 \,, \tag{A.6}$$

where $J_\parallel \equiv \sum_j q_j \mathcal{M}_j^{(1)}$ and we have exploited the fact that the collision operator conserves particle number (for each species independently). We can proceed in a similar fashion using Eq. (A.2) to obtain the evolution equations for higher-order velocity moments; straightforward algebra shows that

$$\left(\frac{\partial}{\partial t} + \mathbf{V}_E \cdot \boldsymbol{\nabla}\right) J_\parallel + \widehat{\mathbf{b}} \cdot \boldsymbol{\nabla} P - n_0 \xi \boldsymbol{\mathcal{M}} \cdot \boldsymbol{\kappa} - (\sigma + \sigma_0) E_\parallel = \sum_j q_j C_j^{(1)} \,, \tag{A.7}$$

and

$$\left(\frac{\partial}{\partial t} + \mathbf{V}_E \cdot \boldsymbol{\nabla}\right) P + \widehat{\mathbf{b}} \cdot \boldsymbol{\nabla} Q - n_0 \xi \mathbf{V}_E \cdot \boldsymbol{\kappa} - 2\widehat{\sigma} E_\parallel = \sum_j q_j C_j^{(2)} \,, \tag{A.8}$$

where $\sigma_0 \equiv n_0 \sum_j q_j^2 / m_j$, $\sigma \equiv \sum_j q_j^2 M_j^{(0)} / m_j$, $\widehat{\sigma} \equiv \sum_j q_j^2 M_j^{(1)} / m_j$, $\xi \equiv \sum_j q_j T_j (1+\eta_j)/m_j$, $\boldsymbol{\mathcal{M}} \equiv \boldsymbol{\nabla} A_\parallel \times \mathbf{B}_0 / B_0^2$ is the magnetic flutter, $P \equiv \sum_j q_j M_j^{(2)}$ is the pressure density and $Q \equiv \sum_j q_j M_j^{(3)}$ is the heat flux density. In order to determined the evolution equations for Φ, $E_\parallel$ and $\partial\psi/\partial t$, we make use of the gyro-kinetic Poisson equation (in the long wavelength)

$$\frac{e^2}{T_e} n_0 \rho_s^2 \nabla_\perp^2 \Phi = -\rho \,, \tag{A.9}$$

and Ampère's law

$$\nabla_\perp^2 A_\parallel = -\frac{4\pi}{c} J_\parallel \,. \tag{A.10}$$

We note that the parallel gradient of a perturbed quantity $\widetilde{f}$ can be written as

$$\widehat{\mathbf{b}} \cdot \boldsymbol{\nabla} \widetilde{f} = \widehat{\mathbf{b}}_0 \cdot \boldsymbol{\nabla} \widetilde{f} + \boldsymbol{\mathcal{M}} \cdot \boldsymbol{\nabla} \widetilde{f} \equiv \nabla_\parallel \widetilde{f} + B_0^{-1} \left[\widetilde{f}, A_\parallel\right] \,,$$

where $[\widetilde{f}, A_\parallel] \equiv \widehat{\mathbf{b}}_0 \cdot (\boldsymbol{\nabla} \widetilde{f} \times \boldsymbol{\nabla} A_\parallel)$ denotes the Poisson bracket for the pair $(\widetilde{f}, A_\parallel)$. In the context of the one-dimensional model used here, it should be noted that $[\widetilde{f}, \widetilde{g}] \equiv 0$ for any

perturbed quantities $\widetilde{f}$ and $\widetilde{g}$; it follows immediately that the parallel gradient of $\widetilde{f}$ takes the simple form of

$$\widehat{\mathbf{b}}\cdot\boldsymbol{\nabla}\widetilde{f}=\widehat{\mathbf{b}}_0\cdot\boldsymbol{\nabla}\widetilde{f}=\nabla_{\parallel}\widetilde{f}. \tag{A.11}$$

In the simple one-dimensional model, the above expression is valid for any perturbed quantity $\widetilde{f}$; in the general (two- or three-dimensional) case, however, Eq. (A.11) does not apply. The equation governing $E_{\parallel}=-\widehat{\mathbf{b}}\cdot\boldsymbol{\nabla}\psi=-\widehat{\mathbf{b}}\cdot\boldsymbol{\nabla}\Phi-\frac{1}{c}\,\partial A_{\parallel}/\partial t$ can be obtained from Eqs. (A.9) and (A.10)

$$\nabla_{\perp}^2 E_{\parallel}=\frac{T_e}{e^2 n_0\rho_s^2}\,\widehat{\mathbf{b}}\cdot\boldsymbol{\nabla}\rho+\frac{4\pi}{c^2}\,\frac{\partial J_{\parallel}}{\partial t}\ ,$$

which, when combined with Eq. (A.7), yields an Helmholtz-like equation

$$\left[\nabla_{\perp}^2-\frac{4\pi}{c^2}\,(\sigma+\sigma_0)\right]E_{\parallel}=\frac{T_e}{e^2 n_0\rho_s^2}\,\widehat{\mathbf{b}}\cdot\boldsymbol{\nabla}\rho+\frac{4\pi}{c^2}\,\left(\xi n_0\boldsymbol{\mathcal{M}}\cdot\boldsymbol{\kappa}+\sum_j q_j C_j^{(1)}-\nabla_{\parallel}P\right). \tag{A.12}$$

In deriving Eq. (A.12) we have made use of the fact that, in this simple one-dimensional model, the parallel gradient operator ($\widehat{\mathbf{b}}\cdot\boldsymbol{\nabla}$) and the perpendicular Laplacian operator ($\nabla_{\perp}^2$) commute (this is not true in the general three-dimensional case). Introducing the intermediary scalar field $\varpi\equiv\partial E_{\parallel}/\partial t$, taking the time derivative of Eq. (A.12) and using Eqs. (A.6)-(A.8), we obtain the following elliptic (Helmholtz-type) equation

$$\left[\nabla_{\perp}^2-\frac{4\pi}{c^2}\,(\sigma+\sigma_0)\right]\varpi=\frac{4\pi}{c^2}\,\nabla_{\parallel}^2 Q-\frac{T_e}{e^2 n_0\rho_s^2}\,\nabla_{\parallel}^2 J_{\parallel}-\frac{4\pi n_0\xi\kappa_n}{c\theta B_0}\,\nabla_{\parallel}E_{\parallel}+S_{\mathrm{NL}}+S_{\mathrm{c}}, \tag{A.13}$$

where

$$S_{\mathrm{c}}=\frac{4\pi}{c^2}\,\left[\frac{\partial}{\partial t}\,\sum_j q_j C_j^{(1)}-\nabla_{\parallel}\left(\sum_j q_j C_j^{(2)}\right)\right],$$

arises dues to the collisional effects, and

$$S_{\mathrm{NL}}=\frac{4\pi}{c^2}\,\left[\left(\sigma_0\mathbf{V}_E\cdot\boldsymbol{\kappa}-\nabla_{\parallel}\widehat{\sigma}\right)E_{\parallel}-2\nabla_{\parallel}\left(\widehat{\sigma}E_{\parallel}\right)\right],$$

accounts for quadratic nonlinearities in the parallel electric field. Finally we must determine the elliptic equation governing $\chi\equiv(1/c)\partial A_{\parallel}/\partial t$; taking the time derivative of Ampère's law, Eq. (A.10), and using Eq. (A.7), the required equation is found to be

$$\nabla_{\perp}^2\chi=\frac{4\pi}{c^2}\,\left[\nabla_{\parallel}P-n_0\xi\boldsymbol{\mathcal{M}}\cdot\boldsymbol{\kappa}-(\sigma+\sigma_0)E_{\parallel}-\sum_j q_j C_j^{(1)}\right]. \tag{A.14}$$

Solving Eqs. (A.12) and (A.13) for $E_\parallel$ and ϖ, respectively, one can determine the scalar fields ψ and $\varphi \equiv \partial\psi/\partial t$ according to

$$\psi(y,t) = -\theta^{-1}\int^y E_\parallel(y',t)dy',$$
$$\varphi(y,t) = \frac{\partial\psi}{\partial t} = -\theta^{-1}\int^y \varpi(y',t)dy',$$

where we have used the expression for the parallel gradient along the *equilibrium* magnetic field, $\nabla_\parallel \widetilde{f} = \theta\partial\widetilde{f}/\partial y$. Using $F_j = e^{-q_j\psi/T_j}F_{Mj} + h_j$ the velocity moments of the perturbed distribution, Eq. (A.5) can be written as:

$$M_j^{(k)} = \left(e^{-q_j\psi/T_j} - 1\right)\int_{-\infty}^{+\infty} F_{Mj}{v_\parallel}^k dv_\parallel + \int_{-\infty}^{+\infty} h_j {v_\parallel}^k dv_\parallel .$$

In gyrokinetic units $[\omega_{ci}t \mapsto t;\ \mathbf{x}/\rho_s \mapsto \mathbf{x};\ v_\parallel/c_s \mapsto v_\parallel;\ e\Phi/T_e \mapsto \Phi;\ e\psi/T_e \mapsto \psi;\ A_\parallel/(\rho_s B_0) \mapsto A_\parallel;\ e\varphi/(\omega_{ci}T_e) \mapsto \varphi;\ \chi/(c_s B_0) \mapsto \chi;\ e\rho_s E_\parallel/T_e \mapsto E_\parallel]$ the field equations can be written as

$$\frac{\partial^2\Phi}{\partial y^2} = (1+1/\tau)\psi + \int_{-\infty}^{+\infty}(h_e - h_i)dv_\parallel - \widehat{\rho}, \tag{A.15}$$

where $\widehat{\rho} = (1+1/\tau)\psi + e^{-\psi/\tau} - e^{\psi} = \mathcal{O}(|\psi|^2)$;

$$\frac{\partial^2 A_\parallel}{\partial y^2} = \beta\int_{-\infty}^{+\infty}(h_e - h_i)v_\parallel dv_\parallel ; \tag{A.16}$$

$$\left(\frac{\partial^2}{\partial y^2} - \eta\right)E_\parallel = \nabla_{||}\int_{-\infty}^{+\infty}(h_i - h_e)dv_\parallel - \beta\nabla_{||}\int_{-\infty}^{+\infty}(h_i - h_e){v_\parallel}^2 dv_\parallel + \beta\left[\xi\kappa_n\frac{\partial A_\parallel}{\partial y} - \sum_j Z_j C_j^{(1)}\right], \tag{A.17}$$

where $\xi = \tau(1+\eta_i) - \epsilon^{-1}(1+\eta_e)$ and

$$\eta \equiv \beta\left(\int_{-\infty}^{+\infty} h_i dv_\parallel + \epsilon^{-1}\int_{-\infty}^{+\infty} h_e dv_\parallel\right) + e^{\psi} + \frac{1}{\tau}\,e^{-\psi/\tau};$$
$$\left[\frac{\partial^2}{\partial y^2} - \beta(\sigma+\sigma_0)\right]\varpi = \nabla_{||}^2\left[\beta\int_{-\infty}^{+\infty}(h_i - h_e){v_\parallel}^3 dv_\parallel - \int_{-\infty}^{+\infty}(h_i - h_e)v_\parallel dv_\parallel\right] - \beta\xi\kappa_n\frac{\partial E_\parallel}{\partial y} + S_c + S_{\mathrm{NL}}, \tag{A.18}$$

where σ_0, σ, S_c, S_{NL} and $\widehat{\sigma}$ are defined by (2.17) and (2.18). Finally,

$$\frac{\partial^2\chi}{\partial y^2} = \beta\nabla_{||}\left[\int_{-\infty}^{+\infty}(h_i - h_e){v_\parallel}^2 dv_\parallel - \kappa_n\xi\frac{\partial A_\parallel}{\partial y} - \sum_j Z_j C_j^{(1)}\right] - \beta\left[\int_{-\infty}^{+\infty} h_i dv_\parallel + \epsilon^{-1}\int_{-\infty}^{+\infty} h_e dv_\parallel\right]E_\parallel . \tag{A.19}$$

B Linear properties of electromagnetic drift waves

Using the formulation of the splitting scheme the distribution function for species j is given by

$$F_j = H_j(\psi) F_{Mj} + h_j, \tag{B.1}$$

where $H_j(\psi) = \exp\left(-q_j\psi/T_j\right)$; substitution of representation (B.1) in the collisionless Vlasov equation, $dF_j/dt = 0$, yields an equation governing the nonadiabatic part of the distribution function

$$\frac{dh_j}{dt} = H_j(\psi)\left[\frac{q_j}{T_j} F_{Mj}\left(\frac{\partial}{\partial t} + \mathbf{V}_E\cdot\boldsymbol{\nabla}\right)\psi - \mathbf{V}_\phi\cdot\boldsymbol{\nabla} F_{Mj}\right], \tag{B.2}$$

where $\mathbf{V}_\phi = c\widehat{\mathbf{b}}_0\times\boldsymbol{\nabla}\phi/B_0$ is the drift velocity associated with the gradient of the generalized potential $\phi \equiv \Phi - v_\parallel A_\parallel/c$. Linearizing Eq. (B.2), and assuming modes of the form $\exp(-i\omega t + i\mathbf{k}\cdot\mathbf{x})$, one gets

$$(-i\omega + ik_\parallel v_\parallel)h_j = \left(-i\omega\frac{q_j\psi}{T_j} - i\omega_\star\frac{e\phi}{T_e}\, g_j(\overline{v}_\parallel)\right) F_{Mj}, \tag{B.3}$$

where $\omega_\star = (k_y\rho_s)c_s/L_n$, $g_j(\overline{v}_{||}) = 1-\eta_j(1-\overline{v}_{||}^{\,2})/2$ and $\overline{v}_{||} = v_\parallel/V_{\mathrm{th}j}$ is the parallel velocity normalized to the thermal velocity. It is convenient to normalize the scalar fields as follows:

$$(\widetilde{\psi},\widetilde{\Phi},\widetilde{\phi}) = e(\psi,\Phi,\phi)/T_e, \qquad \widetilde{A}_\parallel = A_\parallel/(\rho_s B_0).$$

It is easy to show that these definitions are consistent with the normalized velocity $\widetilde{v_{||}} = v_\parallel/c_s$ since $\widetilde{\phi} = \widetilde{\Phi} - \widetilde{v_{||}}\widetilde{A}_\parallel$. However, as we shall take velocity moments of the linear response, it is convenient to write $\widetilde{\phi}$ in terms of $\overline{v}_{||}$ as $\widetilde{\phi} = \widetilde{\Phi} - \alpha_j\overline{v}_{||}\widetilde{A}_\parallel$, where

$$\alpha_j \equiv V_{\mathrm{th}j}/c_s = \sqrt{(T_j m_i)/(T_e m_j)}.$$

We note that $\alpha_i = \sqrt{\tau} = \mathcal{O}(1)$ for the ions, and $\alpha_e = 1/\sqrt{\epsilon} \gg 1$ for the electrons (here $\epsilon \equiv m_e/m_i$ is the electron-to-ion mass ratio and $\tau = T_i/T_e$). Using the linearized form of the parallel electric field, $E_\parallel = -\widehat{\mathbf{b}}_0\cdot\boldsymbol{\nabla}\Phi - (1/c)\partial A_\parallel/\partial t$, one gets $\widetilde{A}_\parallel = (k_\parallel c_s)(\widetilde{\Phi}-\widetilde{\psi})/\omega$, which allows us to write the generalized potential $\widetilde{\phi}$ as

$$\widetilde{\phi} = \frac{\zeta_j - x}{\zeta_j}\,\widetilde{\Phi} + \frac{x}{\zeta_j}\,\widetilde{\psi}, \tag{B.4}$$

where $\zeta_j \equiv \omega/\omega_{\parallel j}$, $\omega_{\parallel j} = \sqrt{2}k_\parallel V_{\mathrm{th}j}$ and $x = \overline{v}_{||}/\sqrt{2}$. Using Eq. (B.4) in Eq. (B.3) we obtain

$$h_j = \frac{\omega_\star}{\omega}\, g_j(x) F_{Mj}\widetilde{\Phi} - i\left(A_{0j} + A_{1j}x + A_{2j}x^3\right)\mathcal{P}^{-1}F_{Mj}\widetilde{\psi}, \tag{B.5}$$

where $A_{0j}=\omega\theta_j$, $A_{1j}=\omega_\star(1-\eta_j/2)/\zeta_j$, $A_{2j}=\omega_\star\eta_j/\zeta_j$, $\theta_j=Z_jT_e/T_j$ and $\mathcal{P}=i\omega(x-\zeta_j)/\zeta_j$. We introduce the k^{th} velocity moment of the nonadiabatic response as

$$M_j^{(k)}\equiv\int_{-\infty}^{+\infty}{v_\parallel}^k h_j dv_\parallel\,. \tag{B.6}$$

Using Eq. (B.5) we find that

$$\begin{aligned}M_j^{(k)}=&n_0(\sqrt{2}V_{\text{th}j})^k\left\{\frac{\omega_\star}{\omega}\left[(1-\eta_j/2)I_k+\eta_jI_{k+2}\right]\widetilde{\Phi}\right.\\&\left.-\frac{1}{\omega_{\parallel j}}\left[A_{0j}Z^{(k)}(\zeta_j)+A_{1j}Z^{(k+1)}(\zeta_j)+A_{2j}Z^{(k+3)}(\zeta_j)\right]\widetilde{\psi}\right\},\end{aligned} \tag{B.7}$$

where

$$I_k\equiv\frac{1}{\sqrt{\pi}}\int_{-\infty}^{+\infty}e^{-x^2}x^k dx\,, \tag{B.8}$$

and

$$Z^{(k)}(\zeta)\equiv\frac{1}{\sqrt{\pi}}\int_{-\infty}^{+\infty}\frac{x^k}{x-\zeta}\,e^{-x^2}dx\,, \tag{B.9}$$

for non-negative integer k. Note that the definition (B.9) for $k=0$ is related to plasma dispersion function of Fried and Conte [14], $Z(\zeta)\equiv Z^{(0)}(\zeta)$. The definite integral (B.8) vanishes for k odd, $I_0=1$ and $I_k=(k-1)!!/2^{k/2}$ for even integer $k\geq 2$ (here $n!!=(n)(n-2)(n-4)\cdots(3)(1)$ for n odd). Substituting the linearized form of Eq. (B.1), $F_j=(1-\theta_j\widetilde{\psi})F_{Mj}+h_j$, in the expression for the charge density one gets

$$\rho=\sum_j q_j\int_{-\infty}^{+\infty}F_j dv_\parallel=-en_0(1+1/\tau)\widetilde{\psi}-n_0\sum_j\frac{q_j}{\omega_{\parallel j}}\,\mathcal{R}(\zeta_j)\widetilde{\psi}. \tag{B.10}$$

Similarly one can calculate the current density as

$$J_\parallel=\sum_j q_j\int_{-\infty}^{+\infty}v_\parallel F_j dv_\parallel=-\frac{n_0}{k_\parallel}\sum_j q_j\left[\omega\theta_j+\zeta_j\mathcal{R}(\zeta_j)\right]\widetilde{\psi}\,, \tag{B.11}$$

where

$$\begin{aligned}\mathcal{R}(\zeta_j)=&A_{0j}Z(\zeta_j)+A_{1j}Z^{(1)}(\zeta_j)+A_{2j}Z^{(3)}(\zeta_j)\\=&\frac{\omega_\star}{\zeta_j}\,(1+\eta_j\zeta_j^2)+Z(\zeta_j)\left[\omega\theta_j+\omega_\star\left(1-\eta_j/2+\eta_j\zeta_j^2\right)\right].\end{aligned} \tag{B.12}$$

The expression for the charge density, Eq. (B.10), and the current density, Eq. (B.11), can be used in the gyrokinetic Poisson equation, $\rho_s^2\nabla_\perp^2\widetilde{\Phi}=-\widetilde{\rho}=-\rho/(en_0)$, and Ampère's law,

$\rho_s^2\nabla_\perp^2\widetilde{A}_\parallel=-\beta\widetilde{J}_\parallel$, where $\widetilde{J}_\parallel=J_\parallel/(en_0c_s)$, to obtain the linear dispersion for electromagnetic drift waves

$$\mathcal{D}(\omega,k)=\omega b+(1-\beta\Omega^2)\left[\omega(1+1/\tau)+\sum_j Z_j\zeta_j\mathcal{R}(\zeta_j)\right]=0, \tag{B.13}$$

where $b=k_\perp^2\rho_s^2$, $\Omega=\omega/(k_\parallel c_s)$ and $\beta=4\pi en_0T_e/B_0^2$. In the electrostatic limit, assuming cold ions ($\zeta_i\gg1$) and warm electrons ($\zeta_e\ll1$), and noting that

$$\zeta_e\mathcal{R}(\zeta_e)\simeq\omega_\star+i\sqrt{\pi}\zeta_e[\omega_\star(1-\eta_e/2)-\omega],$$

and

$$\zeta_i\mathcal{R}(\zeta_i)\simeq-\frac{\omega}{\tau}-\frac{1}{2\zeta_i{}^2}[\omega/\tau+\omega_\star(1+\eta_i)],$$

the dispersion relation (B.13) yields the mode frequency $\omega=\omega_r+i\gamma$ with real frequency and growth rate given by

$$\omega_r=\frac{\omega_\star}{1+b},\quad \gamma\simeq\delta\equiv\sqrt{\frac{\pi}{2}}\frac{\omega_r}{k_\parallel V_{the}}[\omega_\star(1-\eta_e/2)-\omega_r]\ \ (\beta=0). \tag{B.14}$$

In the absence of a background density gradient, $\omega_\star=0$, the dispersion relation (B.13) takes the form of

$$\mathcal{D}(\omega,k)=b+(1-\beta\Omega^2)\Big(1+1/\tau+\tau^{-1}\zeta_iZ(\zeta_i)+\zeta_eZ(\zeta_e)\Big)=0\ (\omega_\star=0), \tag{B.15}$$

which in the cold-ion, warm-electron limit, $\zeta_e\ll1\ll\zeta_i$, yields the kinetic shear Alfvén wave with real mode frequency

$$\omega_r=\pm\omega_A\sqrt{1+b}, \tag{B.16}$$

with a damping rate given by

$$\frac{\gamma}{\omega_A}=-\sqrt{\frac{\pi}{8}}\sqrt{\frac{m_e}{m_i}}\frac{b}{\sqrt{\beta}}. \tag{B.17}$$

Here $\omega_A\equiv(k_\parallel c_s)/\sqrt{\beta}$ is the shear Alfvén wave frequency.

C Energy conservation for a finite-β plasma

We start from the collisionless Vlasov equation written in the form

$$\frac{dF_j}{dt}=\frac{\partial F_j}{\partial t}+\mathbf{V}_{gc}\cdot\boldsymbol{\nabla}F_j+\frac{q_j}{m_j}\widehat{\mathbf{b}}\cdot\mathbf{E}\frac{\partial F_j}{\partial v_{||}}=0, \tag{C.1}$$

where

$$\mathbf{E}=-\boldsymbol{\nabla}\psi=-\boldsymbol{\nabla}\Phi+E_{\|}^{(T)}\widehat{\mathbf{b}}_0,\quad E_{\|}^{(T)}=-(1/c)\partial A_{\|}/\partial t,$$

and the guiding center velocity, $\mathbf{V}_{gc}=v_{||}\widehat{\mathbf{b}}+\mathbf{V}_E$, satisfies $\boldsymbol{\nabla}\cdot\mathbf{V}_{gc}=0$ since $\boldsymbol{\nabla}\cdot\widehat{\mathbf{b}}=\boldsymbol{\nabla}\cdot\mathbf{V}_E=0$ (slab geometry). Noting that $\mathbf{V}_E\cdot\boldsymbol{\nabla}\psi=0$ it follows that

$$\mathbf{V}_{gc}\cdot\boldsymbol{\nabla}\psi=v_{\|}\widehat{\mathbf{b}}\cdot\boldsymbol{\nabla}\psi. \tag{C.2}$$

Operating with $\int v_{\|}^2/2(\bullet)d^3xdv_{||}$ on Eq. (C.1), using $\boldsymbol{\nabla}\cdot\mathbf{V}_{gc}=0$ and Eq. (C.2), we arrive at

$$\frac{\partial}{\partial t}\int\frac{{v_{||}}^2}{2}F_jd^3xdv_{||}+\frac{q_j}{m_j}\int\mathbf{V}_{gc}\cdot\boldsymbol{\nabla}\psi F_jd^3xdv_{||}=0.$$

Multiplying the above equation by m_j, summing over species and using Eq. (C.1), one gets

$$\frac{\partial K}{\partial t}=-\sum_j q_j\int\Phi\frac{\partial n_j}{\partial t}\,d^3x+\sum_j q_j\int\Gamma_jE_{\|}^{(T)}d^3x, \tag{C.3}$$

where $\Gamma_j=\int v_{\|}F_jdv_{\|}$ and

$$K\equiv\sum_j\frac{m_j}{2}\int{v_{||}}^2F_jdv_{||}d^3x, \tag{C.4}$$

is the volume-averaged total kinetic energy. Taking the time derivative of the gyro-kinetic Poisson equation and Ampère's law one can write

$$\frac{\partial K}{\partial t}=\frac{e^2{n_0}{\rho_s}^2}{T_e}\int\Phi\nabla_{\perp}^2\frac{\partial\Phi}{\partial t}\,d^3x+\frac{1}{4\pi}\int\frac{\partial A_{\|}}{\partial t}\,\nabla_{\perp}^2A_{\|}d^3x. \tag{C.5}$$

The last step of the derivation is based on the relation

$$\frac{\partial}{\partial t}\,\boldsymbol{\nabla}\cdot\left(A_{\|}\boldsymbol{\nabla}_{\perp}A_{\|}\right)=\frac{1}{2}\,\frac{\partial}{\partial t}\,\left|\boldsymbol{\nabla}_{\perp}A_{\|}\right|^2+\boldsymbol{\nabla}_{\perp}^2A_{\|}\frac{\partial A_{\|}}{\partial t}\,+\boldsymbol{\nabla}\cdot\left(A_{\|}\frac{\partial}{\partial t}\,\boldsymbol{\nabla}_{\perp}A_{\|}\right) \tag{C.6}$$

and a similar expression for Φ; if follows that Eq. (C.5) can be written as

$$\frac{\partial}{\partial t}\,(K+U+U_{\mathrm{M}})=0, \tag{C.7}$$

where

$$U\equiv\frac{e^2{n_0}{\rho_s}^2}{2T_e}\,\int|\boldsymbol{\nabla}_{\perp}\Phi|^2d^3x \tag{C.8}$$

is the volume-averaged electrostatic field energy and

$$U_{\mathrm{M}}\equiv\frac{1}{8\pi}\,\int\left|\boldsymbol{\nabla}_{\perp}A_{\|}\right|^2d^3x \tag{C.9}$$

is the volume-averaged magnetic field energy.

References

[1] J. L. V. Lewandowski, Plasma Phys. Contr. Fusion 45 (2003) L39.
[2] P. C. Liewer, Nucl. Fusion 25 (1985) 543.
[3] F. Wagner, U. Stroth, Plasma Phys. Contr. Fusion 35 (1993) 1321.
[4] W. Horton, Handbook of Plasma Physics, Vol. 2, Elsevier Science, Amsterdam, 1984.
[5] W. Horton, Rev. Mod. Phys. 71 (1999) 735.
[6] J. Weiland, Collective Modes in Inhomogeneous Plasma, Institute of Physics, Bristol, U.K., 1999.
[7] W. Horton, Phys. Reports 192 (1990) 1; W. Horton, Physica D 2 (1981) 107.
[8] M. Porkolab, R. P. H. Chang, Rev. Mod. Phys. 50(4) (1978) 745.
[9] R. Courant, K. Friedrichs, H. Lewy, Mathematische Annalen 100 (1928) 32.
[10] M. Kotschenreuther, Bull. Am. Phys. Soc. 34 (1988) 2107.
[11] R. E. Denton, M. Kotschenreuther, J. Comput. Phys. 119 (1995) 283.
[12] R. Shanny, J. M. Dawson, J. M. Greene, Phys. Fluids 10 (1967) 1281.
[13] J. L. V. Lewandowski, Phys. Plasmas 12(5) (2005) 2322.
[14] B. D. Fried, S. D. Conte, Plasma Dispersion Function, Academic Press, New York, 1961.
[15] A. Brandt, Math. Comput. 31 (1977) 333.
[16] W. Hackbusch, U. Trottenberg, Lec. Notes Math. 960 (1982) 1.
[17] P. Wesseling, An Introduction to Multigrid Methods, R. T. Edwards Inc., Philadelphia, 2004.
[18] W. L. Briggs, Van Emden Henson, S. F. McCormick, A Multigrid Tutorial, SIAM, 2000.
[19] A. Brandt, Lec. Notes Math. 960 (1982) 220.
[20] F. De la Vallee Poussin, SIAM J. Numer. Anal. 5(2) (1968) 340.
[21] A. Settari, K. Aziz, SIAM J. Numer. Anal. 10(3) (1973) 506.
[22] W. S Press, S. A. Teukolsky, W. T. Vetterling, B. P. Flannery, Numerical Recipes in Fortran, Cambridge University Press, New York, 1992.
[23] G. R. Danesfahani, T. G. Jeans, Electron. Lett. 31(13) (1995) 1032.
[24] C. C. Dyer, J. Comput. Phys. 53(3) (1984) 530.
[25] J. L. V. Lewandowski, Comput. Phys. Commun. 1 (2004) 114.
[26] J. L. V. Lewandowski, Phys. Plasmas 10(8) (2003) 3204.